Microporous and Mesoporous Materials 185 (2014) 30–50

Contents lists available at ScienceDirect

Microporous and Mesoporous Materials

journal homepage: www.elsevier.com/locate/micromeso

Review

The Maxwell–Stefan description of mixture diffusion in nanoporous crystalline materials

Rajamani Krishna *

Van't Hoff Institute for Molecular Sciences, University of Amsterdam, Science Park 904, 1098 XH Amsterdam, The Netherlands

ARTICLE INFO

Article history:
Received 24 July 2013
Received in revised form 21 October 2013
Accepted 29 October 2013
Available online 7 November 2013

Keywords:
Mixture diffusion
Correlation effects
Thermodynamic coupling
Fixed bed adsorbers
Membrane permeation

ABSTRACT

The efficacy of nanoporous crystalline materials in separation applications is often influenced to a significant extent by diffusion of guest molecules within the pores of the structural frameworks. The Maxwell–Stefan (M–S) equations provide a fundamental and convenient description of mixture diffusion. The M–S formulation highlights two separate factors that cause mixture diffusion to be intrinsically coupled: correlation effects, and thermodynamic coupling.

By careful and detailed analyses of a variety of published experimental data on (a) mixture permeation across nanoporous membranes, (b) transient uptake of mixtures within crystals, and (c) transient breakthrough characteristics of fixed bed adsorbers, we identify conditions that require the use of M–S equations including both correlation effects and thermodynamic coupling. Situations are also identified in which either of the coupling effects can be ignored.

Correlation effects cause slowing-down of more-mobile-less-strongly-adsorbed molecules by tardier-more-strongly-adsorbed-partner species; such slowing-down effects are often essential for modeling mixture permeation across nanoporous membranes. Overshoots in the transient uptake of the more mobile partners in single crystals are essentially the consequence of thermodynamic coupling, originating from sizable off-diagonal elements of thermodynamic correction factors Γ_{ij}.

In the case of transient breakthrough of hexane isomers in a fixed bed of MFI zeolite, we show that thermodynamic coupling effects lead to a significant improvement in the separation performance.

Contents

1. Introduction

Ordered crystalline nanoporous materials such as zeolites (crystalline aluminosilicates), metal–organic frameworks (MOFs), zeolitic imidazolate frameworks (ZIFs), covalent organic frameworks (COFs), and porous aromatic frameworks (PAFs) offer considerable potential for a wide variety of separations. The technologies used in such separations are either fixed bed adsorption units (examples listed in Table 1), or membrane permeation devices (examples are listed in Table 2). The separation performance is dictated by a combination of adsorption and diffusion

* Tel.: +31 20 6270990; fax: +31 20 5255604.
E-mail address: r.krishna@uva.nl

1387-1811/$ - see front matter © 2013 Elsevier Inc. All rights reserved.
http://dx.doi.org/10.1016/j.micromeso.2013.10.026

Notation

c_i	molar concentration of species i in gas mixture, mol m^{-3}
c_{i0}	molar concentration of species i in gas mixture at inlet to adsorber, mol m^{-3}
c_t	total pore concentration in adsorbed mixture, mol m^{-3}
$Đ_i$	Maxwell–Stefan diffusivity, m^2 s^{-1}
$Đ_{12}$	M–S exchange coefficient for binary mixture, m^2 s^{-1}
D_i	Fick diffusivity of species i, m^2 s^{-1}
f_i	partial fugacity of species i, Pa
L	length of packed bed adsorber, m
n	number of species in the mixture, dimensionless
N_i	molar flux of species i, mol m^{-2} s^{-1}
p_i	partial pressure of species i in mixture, Pa
p_t	total system pressure, Pa
q_i	component molar loading of species i, mol kg^{-1}
$\overline{q}_i$	spatially averaged component molar loading of species i, mol kg^{-1}
r	radial direction coordinate, m
r_c	radius of crystallite, m
R	gas constant, 8.314 J mol^{-1} K^{-1}
S_{perm}	permeation selectivity, dimensionless
t	time, s
T	absolute temperature, K
u	superficial gas velocity in packed bed, m s^{-1}
v	interstitial gas velocity in packed bed, m s^{-1}
x_i	mole fraction of species i in adsorbed phase, dimensionless
y_i	mole fraction of component i in bulk vapor phase, dimensionless
V_p	pore volume, m^3 kg^{-1}
z	distance along the adsorber, and along membrane layer, m

Greek letters

δ	membrane thickness, m
δ_{ij}	Kronecker delta, dimensionless
ε	voidage of packed bed, dimensionless
Γ_{ij}	thermodynamic correction factors, dimensionless
$[\Gamma]$	matrix of thermodynamic correction factors, dimensionless
μ_i	molar chemical potential, J mol^{-1}
Π_i	permeance of species i in mixture, mol m^{-2} s^{-1} Pa^{-1}
Θ_i	loading of species i, molecules per unit cell
$\Theta_{i,sat}$	saturation loading of species i, molecules per unit cell
Θ_t	total molar loading of mixture, molecules per unit cell
ρ	framework density, kg m^{-3}
τ	dimensionless time, dimensionless

Subscripts

i	referring to component i
t	referring to total mixture

characteristics, that can be manipulated by proper choice of pore size, pore topology, connectivity, and interactions (both van der Waals and electrostatic) of the guest molecules with the framework atoms. While membrane permeation units are commonly operated under steady-state conditions, the operations of fixed bed adsorption units are intrinsically transient in nature, i.e., the gas (or fluid) phase concentrations vary both with distance along the adsorber, z, and time, t [1–3]. The uptake within any crystallite in the fixed-bed adsorber has also a transient character. The description of transient mixture diffusion places a greater burden on process modeling than the corresponding description of steady-state characteristics.

During the last decade, there been a considerable amount of information and insights gained from Molecular Dynamics (MD) simulations to underscore the persuasive advantages in adopting the Maxwell–Stefan (M–S) diffusion equations [4–6], that can be written for a binary mixture as follows

$$-\rho\frac{q_1}{RT}\nabla\mu_1 = \frac{x_2N_1 - x_1N_2}{Đ_{12}} + \frac{N_1}{Đ_1}$$
$$-\rho\frac{q_2}{RT}\nabla\mu_2 = \frac{x_1N_2 - x_2N_1}{Đ_{12}} + \frac{N_2}{D_2}. \quad (1)$$

There are three M–S diffusivities that characterize binary mixture diffusion. The M–S diffusivities: $Đ_1$ and $Đ_2$ portray the interaction of species 1 and 2 with the pore walls. The exchange coefficient, $Đ_{12}$ reflects *correlation* effects in binary mixture diffusion [7].

The chemical potential gradients can be related to the gradients in molar loadings

$$\frac{q_i}{RT}\nabla\mu_i = \sum_{j=1}^{n}\Gamma_{ij}\nabla q_j; \quad \Gamma_{ij} = \frac{q_i}{f_i}\frac{\partial f_i}{\partial q_j}; \quad i,j = 1,....n \quad (2)$$

The elements Γ_{ij} can be determined from models describing mixture adsorption equilibrium such as the Ideal Adsorbed Solution Theory (IAST) [8].

Eqs. (1) and (2) can be combined to yield explicit expression for the fluxes

$$\begin{pmatrix}N_1\\N_2\end{pmatrix} = -\frac{\rho}{1+\frac{x_1Đ_2}{Đ_{12}}+\frac{x_2Đ_1}{Đ_{12}}}\begin{bmatrix}Đ_1\left(1+\frac{x_1Đ_2}{Đ_{12}}\right) & \frac{x_1Đ_1Đ_2}{Đ_{12}}\\ \frac{x_2Đ_1Đ_2}{Đ_{12}} & Đ_2\left(1+\frac{x_2Đ_1}{Đ_{12}}\right)\end{bmatrix}\begin{bmatrix}\Gamma_{11} & \Gamma_{12}\\ \Gamma_{21} & \Gamma_{22}\end{bmatrix}\begin{pmatrix}\nabla q_1\\ \nabla q_2\end{pmatrix}. \quad (3)$$

Eq. (3) demonstrates that there are two different factors that contribute to strong "coupling" in mixture diffusion. Values of $Đ_i/Đ_{12}$ in the range of 1–20 imply strong correlation effects; this results in significant contribution of the off-diagonal elements in the first matrix to the right Eq. (3). Often, but not always, strong correlation effects cause slowing-down of more-mobile-less-strongly-adsorbed molecules by tardier-more-strongly-adsorbed-partner species. Such is the case, for example, for diffusion of H_2/CO_2, CH_4/C_2H_6, CH_4/C_3H_8, and CH_4/nC_4H_{10} mixtures structures such as MFI, FAU, and MgMOF-74 [9]. As illustration, Fig. 1a shows MD simulation data on $Đ_1/Đ_{12}$ for H_2/CO_2 mixtures in MgMOF-74, IRMOF-1, MFI, and LTA-Si, expressed as a function of the total concentration, $c_t = (q_1 + q_2)/V_p$, of the adsorbed mixture within the pores. The use of pore concentrations c_t rather than the molar loadings affords a fairer comparison of different host materials as explained in previous works [4,5,10]. For any guest/host combination, $Đ_1/Đ_{12}$ is seen to increase as the pore concentration increases; this implies that correlation effects are expected to be stronger for separations operating at higher pressures. Correlations are strongest in one-dimensional (1D) channel structures (e.g., MgMOF-74), intersecting channels (e.g., MFI), and "open" structures (e.g., IRMOF-1, FAU, NaX) consisting of large cages separated by wide windows. For such cases, the more

Table 1
Examples of PSA separations using ordered nanoporous crystalline materials. The four categories of materials A, B, C, and D are explained in the main text. Detailed analysis, including breakthrough simulations for each of the separations listed here are provided in the Supplementary material.

Process	Mixtures	Category of materials	Literature
Natural gas purification	CH_4/CO_2 $CH_4/CO_2/H_2S$ $CH_4/CO/CO_2$	**A**: NaX, Cu-TDPAT, MgMOF-74, NiMOF-74, CuBTC, UTSA-16, SIFSIX-2-Cu, MIL-47(V), amino-MIL-53, Amino-MIL-125(Ti), MIL-100(Cr), MIL-140(Zr) **B**: LTA-5A, SAPO-34, KFI	[50,51,58,66,68,70,90,113–119]
Natural gas upgrading for meeting pipeline specifications	N_2/CH_4	**C**: LTA-4A, ETS-4, BaETS-4	[38–40,120]
Recovery of H_2 from steam methane reformer off-gas (SMROG)	H_2/CO_2, $H_2/CO/CH_4/CO_2$ $H_2/CH_4/CO_2$	**A**: MgMOF-74, MOF-177, NaX, CuBTTri, Cu-TDPAT, SIFSIX-2-Cu, Cu-TDPAT, Zn(bdc)dabco,UiO-66, UiO-67, ZJU-35a, ZJU-36a **B**: LTA-5A	[60,66,70–72,114,116,121]
CO_2 capture from flue gas	N_2/CO_2 $N_2/CO_2/CO/O_2$ $N_2/CO_2/SO_2$	**A**: MFI, MgMOF-74, NiMOF-74 NaX, MOF-177, EMC-1, SIFSIX-2-Cu, PCP-1, NOTT-300 **B**: LTA-5A	[49,68,116,122–125]
CO_2 capture from ambient air	$CO_2/O_2/N_2$	**A**: mmen-CuBTTri, PPN-6, mmen-Mg_2(dobpdc)	[126–128]
Fischer–Tropsch tail gas separation	$H_2/CO_2/CO/CH_4/N_2$	**A**: Cu-TDPAT, CuBTC, NaX, MFI **B**: LTA-5A	
Recovery of He from natural gas	$He/N_2/CH_4/CO_2$	**A**: CuBTC, MFI	
Recovery of Xe and Kr from process off-gases	$Xe/Kr/N_2/CO_2$	**A**: NiMOF-74	[79]
Separation of hexane isomers for production of 92+ RON product	*n*C6/2MP/3MP/22DMB/23DMB	**B**: $Fe_2(BDP)_3$, ZIF-77, UiO-66, Zn(bdc)dabco, ATS, CFI, MWW, Co(BDP), ZnMOF-74, MgMOF-74 **C**: ZIF-8 **D**: MFI	[56,87,99]
Separation of C8 hydrocarbons	o-xylene/m-xylene/p-xylene/ethylbenzene	**A**: BaX, Co(BDP), MIL-47, MIL-53, MgMOF-74, NiMOF-74, MIL-125(Ti), Amino-MIL-125(Ti) **B**: UiO-66, Zn(bdc)dabco	[52,91,92,110,129–133]
Separation of C8 hydrocarbons	Ethylbenzene/styrene	**A**: MIL-47, MIL-53	[134,135]
Separation of aromatics from non-aromatics	Benzene/cyclohexanebenzene/n-hexane	**A**: Na-Y, Pd-Y, Ag-Y, H-USY, PAF-2	[136,137]
Separation of alkene/alkane	C_2H_4/C_2H_6 C_3H_6/C_3H_8 1-octene/nC8	**A**: CuBTC, MgMOF-74, NiMOF-74, CoMOF-74, NaX **B**: ZIF-7, ZIF-8	[3,55,57,75,78,138–140]
Separation of C1, C2, C3 hydrocarbons	$CH_4/C_2H_2/C_2H_4/C_2H_6/C_3H_6/C_3H_8$	**A**: M'MOFs,MgMOF-74, CoMOF-74,FeMOF-74, CuBTC, UTSA-30a, UTSA-35a	[3,55,141–143]
Production of C_2H_2	CO_2/C_2H_2	**A**: UTSA-30a, UTSA-50a, CuBTC	[143–146]
Separation of C4 hydrocarbons	*n*C4/iC4	**A**: CuBTC	[80]
Separation of butenes	is-2-butene/trans-2-butene/1-butene	**B**: RUB-41 zeolite	[85]
Removal of dienes from C4 gas stream	1,3 butadiene/1-butene	**A**: Ag-Y zeolite	[147]
Dehydration of alcohols	Water/ethanol	**B**: LTA-K, LTA-Na, LTA-Ca, FAU-Na	[148]
Separation of 1-alcohols	Methanol/ethanol/1-propanol/1-butanol/1-hexanol	**D**: SAPO-34	[45,46,94]
Production of pure O_2	N_2/O_2	**A**: LiX, LiLSX **B**: LTA-5A	[81–84,149]
Production of pure N_2	N_2/O_2	**A**: FeMOF-74 **C**: LTA-4A	[95–97]
Separation of chlorofluorocarbons	CFC-115/HFC-125	**D**: MFI	[150]

mobile species is slowed down significantly by the tardier partner. The influence of correlations is best illustrated by the MD simulation data [11,12] presented in Fig. 1b on the self-diffusivities of H_2 and CO_2 in H_2/CO_2 mixtures of varying composition of CO_2 in the adsorbed phase. We note the severe reduction, by a factor of five, of the self-diffusivity of H_2 with increasing amount of CO_2 within the channels of MFI. The more strongly adsorbed CO_2 does not vacate adsorption sites quick enough for H_2 to occupy. Consequently, there is a slowing-down of the more mobile H_2 in the mixture. The self-diffusivity of CO_2 is influenced to a much smaller extent. Generally speaking, correlation effects have a strong *retarding* influence of the permeation of more-mobile-less-strongly-adsorbed molecules. Conversely, correlation effects are of lesser importance for tardier-more-strongly-adsorbed species.

For the special case of *dominant* correlations, i.e., $Đ_1/Đ_{12} \to \infty; Đ_2/Đ_{12} \to \infty$, we can derive the following simple flux expressions [13]

$$\begin{pmatrix} N_1 \\ N_2 \end{pmatrix} = -\frac{\rho}{\frac{x_1}{Đ_1}+\frac{x_2}{Đ_2}} \begin{bmatrix} x_1 & x_1 \\ x_2 & x_2 \end{bmatrix} \begin{bmatrix} \Gamma_{11} & \Gamma_{12} \\ \Gamma_{21} & \Gamma_{22} \end{bmatrix} \begin{pmatrix} \nabla q_1 \\ \nabla q_2 \end{pmatrix}; \quad \text{correlations dominant} \tag{4}$$

The *dominant* correlations scenario provides an excellent description of mixture diffusion in carbon nanotubes [6,13,14].

Extensive Molecular Dynamics (MD) simulations have shown that correlation effects are of negligible importance for mixture diffusion within materials such as ZIF-8, CHA, LTA, DDR, ERI that consist of cages separated by windows in the 3.4–4.2 Å size range [4,5,9,15]; molecules jump one-at-a-time across the narrow windows, and the assumption of negligible correlations is often justified. The experimental data of Chmelik et al. [16] on self-, M–S, and Fick diffusivities of methanol, ethanol, and ethane in ZIF-8 provide direct experimental verification of the absence of correlations in such structures. Values of $Đ_i/Đ_{12} \to 0$, imply negligible influence of correlations; in this case, the first members on the right of Eq. (1) can be ignored, yielding

Table 2
Examples of nanoporous membrane separations. **Category E** represents materials for which correlation effects and thermodynamic coupling effects are both of importance. **Category F** represents materials for which correlation effects are of minor significance. Detailed analysis, including membrane permeation simulations for each of the separations listed here are provided in the Supplementary material.

Process	Mixtures	Category of materials	Literature
CO_2 capture from flue gas	CO_2/N_2	**E**: NaY, NaX, MFI, ZIF-69 **F**: SAPO-34, DDR	[25,151–155]
CO_2 removal for natural gas purification	CO_2/CH_4	**E**: MFI, NaY, NaX, MgMOF-74, amino-MIL-53, ZIF-69 **F**: SAPO-34, ZIF-8, DDR	[9,11,12,24,25,151,154,156–159]
N_2 removal for natural gas purification	N_2/CH_4	**F**: SAPO-34, DDR	[25,151]
CO_2-selective purification of H_2	H_2/CO_2	**E**: MFI, NaX, MgMOF-74, **F**: SAPO-34	[9,11,12,19,152]
H_2-selective purification of H_2	H_2/CO_2	**E**: amino-MIL-53(Al) **F**: ZIF-7, ZIF-22	[160–162]
H_2-selective separation from hydrocarbons	H_2/CH_4 H_2/C_3H_8	**E**: amino-MIL-53(Al) **F**: ZIF-7, ZIF-8, ZIF-22, SAPO-34	[25,160–164]
Alkene/alkane	C_2H_4/C_2H_6 C_3H_6/C_3H_8	**E**: NaY, FeMOF-74 **F**: ZIF-7, ZIF-8	[27–29,55,165]
Pervaporation	Water/methanol Water/ethanol Water/2-propanol Water/NMP	**E**: MFI **F**: LTA-4A, CHA, H-SOD, DDR, ZIF-8	[166–169]
Separation of light alkanes	$CH_4/C_2H_6/C_3H_8$	**E**: MFI	[20]
Separation of C4 hydrocarbons	iC4/1-butene nC4/iC4	**E**: MFI	[35,170,171]
Separation of C5 hydrocarbons	nC5/isoprene	**E**: MFI	[172]
Separation of hexane isomers	nC6/2MP nC6/22DMB	**E**: MFI	[34,47,173–175]
Separation of C8 hydrocarbons	o-xylene/m-xylene/p-xylene/ethylbenzene	**E**: MFI	[35,174]
Separation of aromatics from aliphatics	Benzene/nC6 Benzene/nC7 benzene/cyclohexane	**E**: NaY, NaX	[22,176]

$$\begin{pmatrix} N_1 \\ N_2 \end{pmatrix} = -\rho \begin{bmatrix} Đ_1 & 0 \\ 0 & Đ_2 \end{bmatrix} \begin{bmatrix} \Gamma_{11} & \Gamma_{12} \\ \Gamma_{21} & \Gamma_{22} \end{bmatrix} \begin{pmatrix} \nabla q_1 \\ \nabla q_2 \end{pmatrix}; \text{ negligible correlations} \quad (5)$$

While there are a large number of publications that highlight the significance of correlation effects in mixture diffusion [12,17,18], far fewer publications are devoted to highlighting the influence of "thermodynamic coupling", originating from contributions of sizable off-diagonal elements of $[\Gamma]$.

In the special case of dilute mixtures and operations at low loadings, we may invoke the simplification $\Gamma_i = \delta_{ij}$, the Kronecker delta, signifying absence of thermodynamic coupling:

$$\begin{pmatrix} N_1 \\ N_2 \end{pmatrix} = -\rho \begin{bmatrix} Đ_1 & 0 \\ 0 & Đ_2 \end{bmatrix} \begin{bmatrix} 1 & 0 \\ 0 & 1 \end{bmatrix} \begin{pmatrix} \nabla q_1 \\ \nabla q_2 \end{pmatrix}; \text{ negligible correlations; no thermo coupling} \quad (6)$$

The differences in the estimations using Eqs. (5) and (6) can be attributed to the influence of thermodynamic coupling.

The major objectives of this article are listed below. By careful detailed analyses of a variety of published experimental data on (a) mixture permeation across nanoporous membranes, (b) transient uptake of mixtures within crystals, and (c) transient breakthrough characteristics of fixed bed adsorbers we identify conditions that require the use of Eq. (3) including both correlation effects and thermodynamic coupling. We aim to demonstrate that thermodynamic coupling effects, originating from finite off-diagonal elements of $[\Gamma]$, are of particular importance in *transient* permeation, uptake and breakthroughs. In the case of the separation of hexane isomers in a fixed-bed of MFI zeolite, we shall show that inclusion of thermodynamic coupling effects leads to a significant improvement in the separation performance. We identify situations in which the uncoupled Eq. (6), ignoring both correlations and thermodynamic coupling, are of adequate accuracy for use in practice. Furthermore, we also identify situations and conditions in which intra-crystalline diffusion effects have a negligible influence the separation performance.

The Supplementary material, accompanying this article includes (a) detailed derivation of the Maxwell–Stefan equations for mixture diffusion, (b) characteristics of the M–S diffusivities and procedures for estimation of correlations, (c) numerical procedures used for simulation of transient uptake within single crystals, transient breakthrough in fixed bed adsorbers, transient permeation across nanoporous membranes, (d) molecular simulation methodology and data for alkane isomers in MFI zeolite, and (e) detailed comparisons of experimental data on uptake, breakthrough and membrane permeation with simulation results.

2. Correlation effects in binary mixture permeation across membranes

Generally speaking, intra-crystalline diffusion effects are of greater significance for membrane permeation than for transient breakthrough in fixed-bed adsorbers. The influence of correlations is best illustrated by considering the experimental data of Sandström et al. [19] for permeances of H_2 and CO_2 in a MFI membrane, determined both from unary and binary mixture permeation data; see Fig. 1c. The permeance of species i is defined as the permeation flux N_i divided by the trans-membrane partial pressure difference, Δp_i

$$\Pi_i \equiv \frac{N_i}{\Delta p_i} \quad (7)$$

We note that the permeance of the tardier CO_2 in the mixture is nearly the same as that for unary permeation for the entire range of upstream (feed) partial pressures. For H_2, the permeance in the mixture is about an order of magnitude lower than from unary experiments. The reduction of the permeance of H_2 in the H_2/CO_2 mixtures is the consequence of two separate factors. Firstly, the mixture adsorption favors the more strongly adsorbed CO_2. Secondly, the mobility of H_2 in the mixture is reduced due to

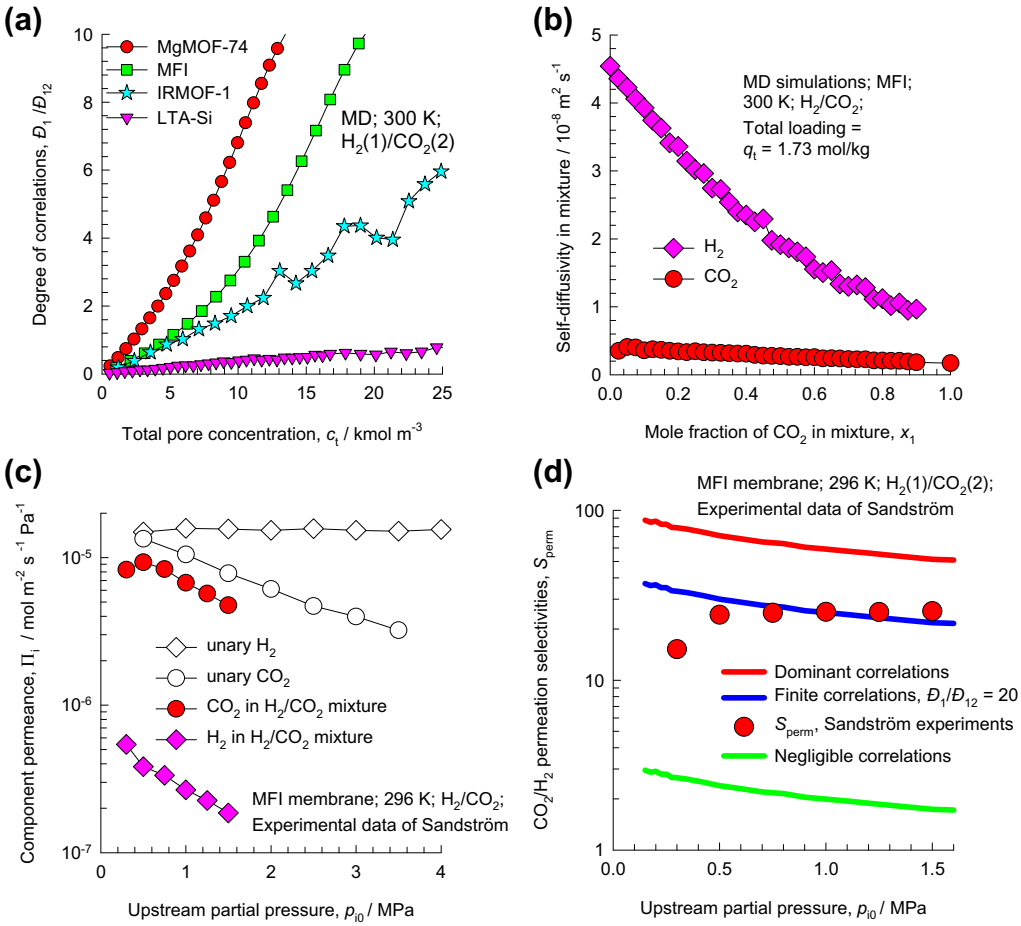

Fig. 1. (a) MD simulation data for the degree of correlations, $Đ_1/Đ_{12}$, for diffusion of equimolar binary ($c_1 = c_2$) H_2/CO_2 mixtures at 300 K in MgMOF-74, MFI, IRMOF-1, and LTA-Si, as a function of the total pore concentration, $c_t = (q_1 + q_2)/V_p$. (b) MD simulations of the self-diffusivities of H_2 and CO_2 in binary mixtures at 300 K in MFI zeolite for a total loading of 1.73 mol/kg. (c) Permeances of H_2 and CO_2 determined for unary and binary mixture permeation across MFI membrane. The graph is constructed using the data of Sandström et al. [19] (d) Comparison of experimental CO_2/H_2 permeation selectivities with M–S model, using three different scenarios for correlations [9].

correlation effects in mixture diffusion, illustrated in Fig. 1b. This implies that mixture permeation is CO_2-selective, whereas the data based on unary permeation demonstrates H_2-selective characteristics.

Calculations using Eq. (3), taking $Đ_1/Đ_{12} = 20$, along with the values of $\rho Đ_1/\delta = 80$ kg m^{-2} s^{-1}, $\rho Đ_2/\delta = 2.7$ kg m^{-2} s^{-1}, both determined from unary permeation data are shown in Fig. 1d. There is good agreement of model calculations with the experimentally determined permeation selectivities, S_{perm}, defined by

$$S_{\text{perm}} = \frac{\Pi_1}{\Pi_2} = \frac{N_1/\Delta p_1}{N_2/\Delta p_2} \tag{8}$$

In order to underscore the significant influence of correlations, Fig. 1d also present the model calculations using Eq. (5), in which correlations are considered negligible. This simplified scenario, using Eq. (5), under-estimates the S_{perm} by about an order of magnitude. The *dominant* correlations scenario, Eq. (4), tends to overestimate the CO_2/H_2 permeation selectivity; see Fig. 1d. Membrane materials with high degrees of correlation are the best choices for enhancing the CO_2/H_2 permeation selectivity. Conversely, if we require the membrane to be selective to H_2 permeation, the best choices are materials such as ZIF-7, ZIF-8 in which correlation effects are of negligible importance.

Consider the experimental data of van de Graaf et al. [20] for permeation of CH_4/C_2H_6 mixtures across an MFI membrane,

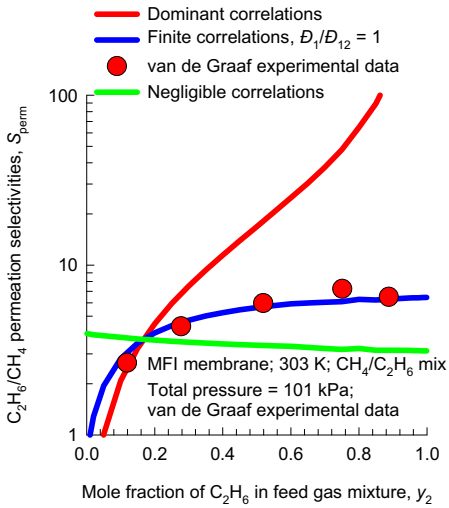

Fig. 2. Experimental data of van de Graaf et al. [20] for the permeation selectivities of CH_4/C_2H_6, and mixtures as a function of the mole fraction of the tardier component in the feed gas mixture. The total pressure at 101 kPa. Three different scenarios for correlations are compared with experimental data on permeation selectivities. The model for calculation of the permeation fluxes and permeances is based on a simplified analytic solution [9]. The Supplementary material provides further simulation details.

presented in Fig. 2. The experimental C_2H_6/CH_4 permeation selectivities data are plotted as functions of the mole fraction of the tardier component in the feed gas mixture in the upstream compartment. Increasing the proportion of the tardier component in the feed mixture has the effect of progressively increasing S_{perm}. The reasons are twofold: (a) due to mixture adsorption equilibrium that favors the heavier alkane, and (2) slowing-down of the mobility of CH_4 due to correlation effects. Ignoring correlation effects, and using the flux Eq. (5) severely underestimates S_{perm}. The *dominant* correlations scenario, Eq. (4), tends to overestimate the C_2H_6/CH_4 permeation selectivity. Use of the flux Eq. (3) including finite correlation effects with $Đ_1/Đ_{12} = 1$ provides good estimates of S_{perm} in accord with experiments, over the entire range of compositions in the upstream compartment.

Baertsch et al. [21] have compared component permeances of o-xylene, m-xylene, p-xylene, ethylbenzene, toluene, and benzene across MFI membrane obtained from unary permeation experiments with those determined from a variety of binary mixture permeation data. The component permeances for mixed gas permeation was found to coincide with the permeance of the tardier species in the binary mixtures; this is clear demonstration of slowing-down of the more mobile partner species. Several other examples of the influence of correlations on mixture diffusion available in the literature [4,5,9].

Jeong et al. [22] report permeances of benzene and cyclohexane across a NaY zeolite membrane, obtained from both unary and mixture permeation experiments. The adsorption selectivity is strongly in favor of benzene, whereas the diffusion selectivity favors cyclohexane. The lower diffusivity of benzene is most likely attributable to the much stronger binding energy of benzene with the cations in NaY [23]. From unary permeation data we note that the membrane is selective to cyclohexane. However, the mixture permeation is selective to benzene. Correlation effects tend to slow down the more mobile cyclohexane and the permeation selectivity is largely governed by adsorption selectivity that favors benzene.

Generally speaking, correlation effects are of minor significance for mixture permeation across SAPO-34, ZIF-8, DDR, and LTA membranes [9,24–26]; we shall demonstrate this by examining some experimental data.

Consider permeation of CO_2/CH_4 separation using a membrane made up of thin layers of SAPO-34 that consists of 316 Å^3 sized cages separated by 3.8 Å × 4.2 Å sized windows. Both adsorption and diffusion selectivities are in favor of CO_2. Experimental data on permeances Π_i of CO_2 and CH_4 determined from binary permeation experiments [24–26] are compared in Fig. 3a and b, with the M–S model estimations (denoted by continuous solid lines) using flux Eq. (5), ignoring correlations. In this case, $(Đ_1/Đ_{12}) \to 0$ is a good assumption to make.

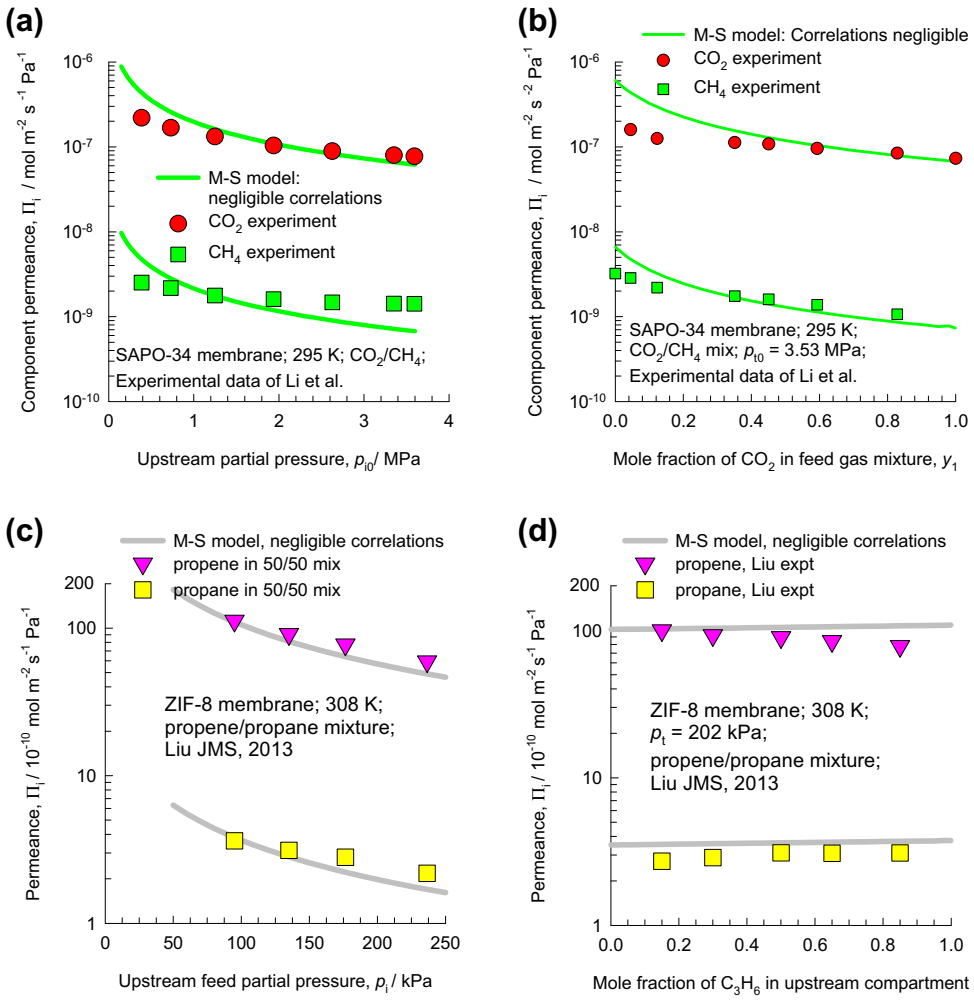

Fig. 3. (a, b) Experimental data [24–26] on permeances of CO_2(1) and CH_4(2) for binary mixture permeation across SAPO-34 membrane at 295 K. (c, d) Experimental data [29] on permeances of C_3H_6(1), and C_3H_8(2) for binary mixture permeation across ZIF-8 membrane at 308 K. In (a), and (c) the upstream compartment consists of equmolar mixtures. In (b), and (d) the composition in the upstream compartment is varied, keeping the total upstream pressure constant. The solid lines are estimations based on the flux Eq. (5), ignoring correlations, and using an analytic solution [9]. The Supplementary material provides further simulation details.

The separation of C_2H_4/C_2H_6, and C_3H_6/C_3H_8 mixtures using ZIF-8 membranes [27–29] is primarily based on differences in the diffusivities of the alkenes and alkanes; such differences arise due to subtle differences in bond lengths and bond angles [30]. Experimental data on diffusivities of C_2H_4, and C_2H_6 show diffusion selectivities of the order of 5 in favor of C_2H_4 [27]. The ratio of the diffusivity of C_3H_6 propene to that of C_3H_8 in ZIF-8 has a value of 125 based on the uptake data of Li et al. [31] A further confirmation of the subtle influence of bond lengths and bond angles on diffusivities of alkenes and alkanes is provided by Ruthven and Reyes [32] who report diffusion selectivity values for C_3H_6/C_3H_8 mixtures in excess of 1000 for CHA and DDR zeolites.

The adsorption selectivities for C_2H_4/C_2H_6, and C_3H_6/C_3H_8 mixtures using ZIF-8 favor the saturated alkane; this implies that adsorption and diffusion do not proceed hand in hand. The diffusion selectivities over-ride the adsorption selectivties, yielding permeation selectivities in favor of the unsaturated alkene.

The experiments of Bux et al. [27] for a ZIF-8 membrane show that the C_2H_4/C_2H_6 permeation selectivity is in the range of 2–3. For C_3H_6/C_3H_8 permeation across ZIF-8 membrane, the permeation selectivities, S_{perm}, reported in the experiments of Liu et al. [29] (Fig. 3c and d) show values in the range of 30–35. From the data in Fig. 3d we note that the magnitude of Π_i is hardly influenced by the mixture composition in the upstream compartment; correlation effects have negligible influence. The experimental data on component permeances for C_3H_6/C_3H_8 mixture permeation are adequately described by the M–S model estimations (denoted by continuous solid lines) using flux Eq. (5).

3. Overshoot phenomena in transient membrane permeation

Diffusional coupling effects often lead to unusual phenomena such as overshoots in the flux of the more mobile partners during transient mixture permeation across nanoporous membranes. Geus et al. [33] report experimental data on transient permeation CH_4/nC_4H_{10} mixture across MFI in which the flux of the more mobile CH_4 exhibits a pronounced maximum during the initial stages of the transience. In order to rationalize their experimental results we carried out simulations to determine the transient permeation fluxes by solving the set of partial differential equations

$$\frac{\partial q_i(z,t)}{\partial t} = -\frac{1}{\rho}\frac{\partial}{\partial z}(N_i) \tag{9}$$

where z is the distance coordinate along the direction of membrane thickness.

The simulation results for transient permeation CH_4/nC_4H_{10} mixture are shown in Fig. 4a–c for three different scenarios. In the simulations presented in Fig. 4a we use the flux Eq. (3), including both correlations and thermodynamic coupling. The flux of the more mobile-less-strongly-adsorbed-CH_4 shows a pronounced maximum, whereas the tardier-more-strongly-adsorbed- nC_4H_{10} exhibits a monotonous approach to steady-state. In the simulations presented in Fig. 4b we use the flux Eq. (5), ignoring correlations, but including thermodynamic coupling. In this scenario too, we note that the flux of CH_4 exhibits a maximum during the early phase of the transience. It is noteworthy that the maximum in the flux of CH_4 is more prominent when correlations are ignored. This is because correlations tend to slow down the more mobile CH_4. Ignoring correlations, results in no slowing-down effects, and the steady-state flux of CH_4 is higher than for the scenario in which correlations are included. In the simulations presented in Fig. 4c we use the flux Eq. (6) ignoring correlations and also ignoring thermodynamic coupling, with $\Gamma_{ij} = \delta_{ij}$. In this scenario too we note that the maximum in the CH_4 fluxes vanishes. The maximum in the transient CH_4 flux is traceable to thermodynamic coupling effects; the results presented in Fig. 4a afford the best representations of the experiments of Geus et al. [33].

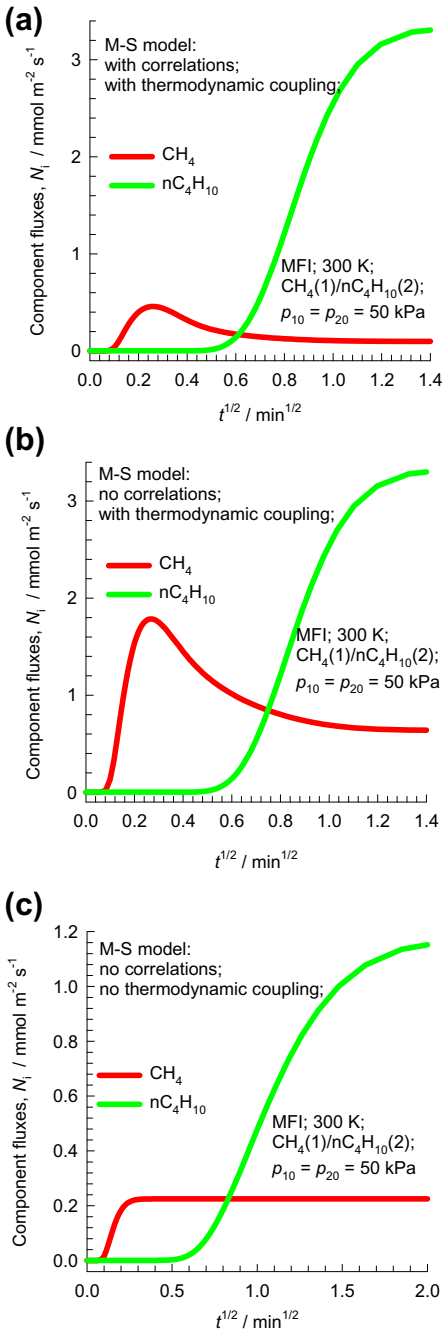

Fig. 4. (a, b, c) Simulations of transient permeation of $CH_4(1)/nC_4H_{10}(2)$ mixture across MFI membrane at 300 K, using three different scenarios for the fluxes. In (a) we use the flux Eq. (3), including both correlations and thermodynamic coupling. In (b) we use the flux Eq. (5), ignoring correlations, but including thermodynamic coupling. In (c) we use the flux Eq. (6) ignoring correlations and also ignoring thermodynamic coupling, with $\Gamma_{ij} = \delta_{ij}$. The Supplementary material provides further simulation details.

For permeation of *n*C6/2MP, and nC6/23DMB mixture across an MFI membrane, Matsufuji et al. [34] have reported experimental data showing overshoots in the *n*C6 flux during transient approach to steady-state; these maxima are the caused by thermodynamic coupling. The experimental data of Matsufuji et al. [35] for transient pervaporation of binary m-xylene/p-xylene, and ternary p-xylene/m-xylene/o-xylene mixtures across MFI membrane show a maximum in the flux of p-xylene which is the most mobile of

the three isomers; the origin of the maximum in the flux of p-xylene can be traced to the influence of thermodynamic coupling. For permeation of benzene/p-xylene mixtures across an MFI membrane, Kolvenbach et al. [36] have reported an overshoot of the benzene flux during the early stages of the transience. For *n*C4/iC4 mixture permeation across a MFI membrane, curious overshoots, and undershoots, in the transient retentate and permeate concentrations have been reported in the experiments of Courthial et al. [37]; such phenomena are also ascribable to thermodynamic coupling effects.

Generally speaking, diffusional coupling effects have greater influences on transient permeation, than on the steady-state characteristics of membranes.

4. Overshoot phenomena in transient mixture uptake in crystals

We now examine experimental data published in the literature where transient overshoots of the component loading of one of the components for binary mixture uptake within crystals have been reported.

The first example we consider is the separation of N_2/CH_4 mixtures, that is important in the context of natural gas upgrading. For transportation purposes, the pipeline specifications usually demand that the amount of N_2 in natural gas is less than about 3%, because the presence of N_2 reduces the heating value. For purification of natural gas streams, that is commonly available at high pressures, it is desirable to use adsorbents in pressure swing adsorption (PSA) units that are selective to N_2, that is present in quantities that are often as high as 20%. For most known adsorbents, the adsorption selectivity favors CH_4. One practical solution to this problem is to rely on diffusion selectivities by using nanoporous materials that have significantly higher diffusivities of N_2, compared to that of CH_4 [38,39].

The earliest study demonstrating the possibility of utilizing diffusion selectivities for separating N_2/CH_4 mixtures is contained in the classic paper of Habgood [40] that presents experimental data on transient uptake of N_2/CH_4 mixtures in crystallites of LTA-4A; see Fig. 5a. The N_2/CH_4 mixture constitutes a combination of more-mobile-less-strongly-adsorbed-N_2 and tardier-more-strongly-adsorbed-CH_4. The diffusivity of N_2 is a factor 22 higher than that of CH_4, but it has an adsorption strength that is a factor 2.2 lower. During the initial stages of the transient uptake, the pores of LTA-4A are predominantly richer in the more mobile N_2, but this is displaced by the more strongly adsorbed, tardier CH_4 molecules at longer times; this results in an overshoot in the N_2 uptake.

For modeling the transient mixture uptake we need to determine the radial distribution of molar loadings, q_i, within a spherical crystallite, of radius r_c, by solving

$$\frac{\partial q_i(r,t)}{\partial t} = -\frac{1}{\rho}\frac{1}{r^2}\frac{\partial}{\partial r}\left(r^2 N_i\right) \tag{10}$$

At any time t, during the transient approach to thermodynamic equilibrium, the spatially averaged molar loading within the crystallites of radius r_c is calculated using

$$\overline{q}_i(t) = \frac{3}{r_c^3}\int_0^{r_c} q_i(r,t) r^2 dr \tag{11}$$

The $\overline{q}_i(t)$ can be compared directly with experimental transient uptake data. The continuous solid lines in Fig. 5a are the calculations of the M–S model using the flux Eq. (5); this model successfully captures the overshoot in the uptake of the more mobile N_2.

The dashed lines in Fig. 5a are the M–S model simulations using Eq. (6) in which the matrix of thermodynamic correction factors is assumed to be the identity matrix, i.e., taking $\Gamma_i = \delta_{ij}$. Neglect of thermodynamic coupling results in uptake profiles that do not exhibit an overshoot in N_2 uptake. The simulation results presented in Fig. 5a confirm that thermodynamic coupling is the cause of the N_2 overshoot.

The transient uptake data of Majumdar et al. [39] for 10/90, and 50/50 N_2/CH_4 mixtures in Ba-ETS-4 show overshoots in the uptake of the more mobile N_2. As demonstrated by the uptake simulations presented in the Supplementary material, the cause of the overshoot is traceable to thermodynamic coupling effects. The same rationalization holds for the overshoots of the more mobile partners in the uptake of benzene/p-xylene in ZSM-5 [41,42] (cf. Fig. 5b), benzene/ethylbenzene in ZSM-5 [41,42], CH_4/C_2H_6 in LTA-4A [43], and n-heptane/benzene in NaX [44].

The maximum in the ethanol uptake from ethanol/1-propanol mixtures in SAPO-34 [45] (cf. Fig. 5c) deserves special mention. In this case, both adsorption and diffusion favor the more mobile ethanol and this synergistic aspect manifests in the transient breakthrough of 1-alcohol mixtures in fixed bed units [46]. Fig. 5d shows the calculations of ($\Gamma_{12}\ q_2/\Gamma_{11}\ q_1$), and ($\Gamma_{21}\ q_1/\Gamma_{22}\ q_2$), that signify the relative influences of thermodynamic coupling on the uptakes of components 1, and 2, respectively. Uptake of ethanol is strongly influenced by the uptake of 1-propanol. Conversely, the uptake of 1-propanol is oblivious to the uptake of ethanol. We also note that ($\Gamma_{12}\ q_2/\Gamma_{11}\ q_1$) exhibits a maximum at a total uptake $q_t \approx 3$ mol/kg; this is the same loading for which the maximum in the transient uptake of ethanol is observed experimentally. The significant off-diagonal contribution of $\Gamma_{12}\ q_2$ is the root cause of the overshoot in the flux of the more mobile ethanol; detailed simulation results are presented in the Supplementary material.

For uptake of binary *n*C6/3MP and *n*C6/22DMB mixtures in MFI crystals, simulations [47] show overshoots in the uptake of the more mobile *n*C6; this is attributable to thermodynamic coupling. The strong influence of thermodynamic coupling on hexane isomers separation with MFI was first underscored in 1998 [48].

5. Intra-crystalline diffusion influences on transient breakthrough in fixed bed adsorbers

Fixed bed, packed with crystals of nanoporous materials, are commonly used for separation of mixtures (see schematic in Fig. 6); such adsorbers are commonly operated in a transient mode, and the compositions of the bulk fluid phase, and within the crystals, vary with position and time. Experimental data on the transient breakthrough of mixtures across fixed beds are commonly used to evaluate and compare the separation performance of zeolites and MOFs [49–59]. For a given separation task, transient breakthroughs provide a more realistic evaluation of the efficacy of a material, as they reflect the combined influence of adsorption selectivity, and adsorption capacity [60]. Furthermore, transient breakthroughs are influenced by both mixture adsorption equilibrium, and intra-crystalline diffusion. In order to determine the extent of the relative importance of adsorption and diffusion in determining the separation performance we perform transient breakthrough simulations, and compare these with experimental data. Our objective here is to reach conclusions regarding the level of sophistication that is required in properly capturing the transient breakthrough characteristics of fixed bed adsorbers.

Assuming plug flow of an n-component gas mixture through a fixed bed maintained under isothermal conditions, the partial pressures in the gas phase at any position and instant of time are obtained by solving the following set of partial differential equations for each of the species i in the gas mixture [1,2,61–65].

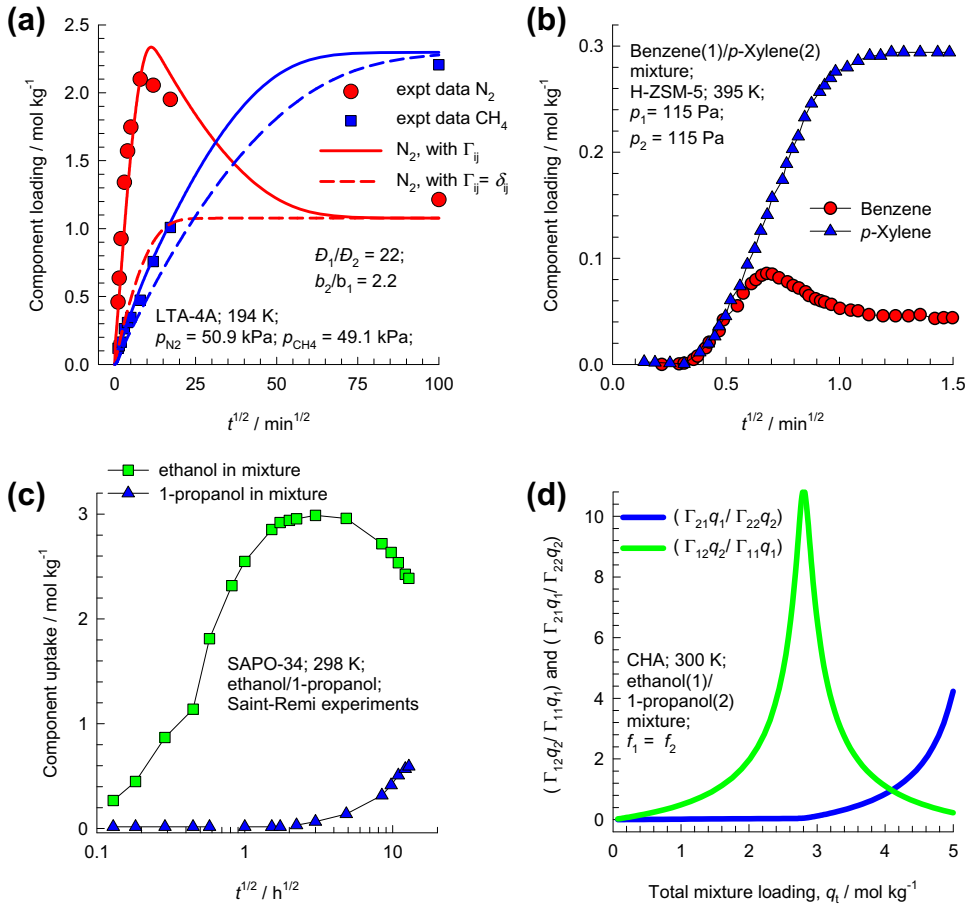

Fig. 5. (a) Experimental data of Habgood [40] on transient uptake of $N_2(1)/CH_4(2)$ mixture within LTA-4A crystals, exposed to binary gas mixtures at partial pressures $p_1 = 50.9$ kPa; $p_2 = 49.1$ kPa at 194 K. The continuous solid lines calculations using Eq. (5) for fluxes. The dashed lines are the calculations using uncoupled flux Eq. (6) with $\Gamma_{ij} = \delta_{ij}$. (b) Experimental data of Niessen and Karge [41,42] for uptake of benzene/*p*-xylene mixtures in MFI zeolite (H-ZSM-5). (c) Experimental data of Saint-Remi et al. [45] for transient uptake of ethanol/1-propanol mixtures within SAPO-34 crystals, that is the structural analog of CHA zeolite. (d) Calculations of $(\Gamma_{12}\, q_2/\Gamma_{11}\, q_1)$, and $(\Gamma_{21}\, q_1/\Gamma_{22}\, q_2)$, for ethanol(1)/1-propanol(2) mixture, expressed as a function of the total mixture loading $q_t = q_1 + q_2$. The Supplementary material provides further simulation details in all cases.

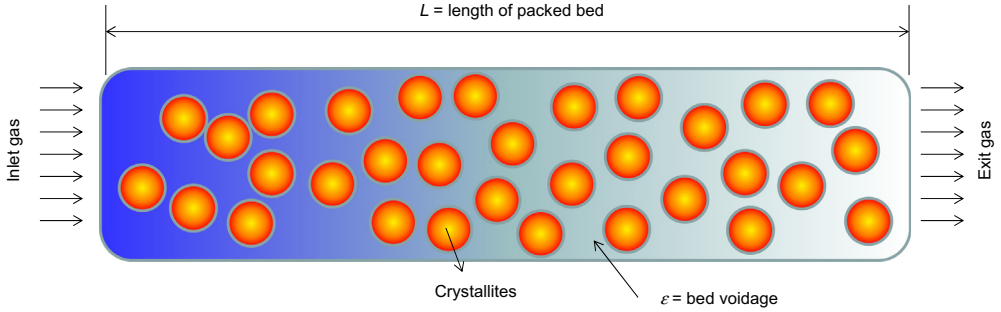

Fig. 6. Schematic of a packed bed adsorber.

$$\frac{1}{RT}\frac{\partial p_i(t,z)}{\partial t} = -\frac{1}{RT}\frac{\partial (v(t,z)p_i(t,z))}{\partial z} - \frac{(1-\varepsilon)}{\varepsilon}\rho\frac{\partial \bar{q}_i(t,z)}{\partial t}; \quad i = 1,2,...n \tag{12}$$

In Eq. (12), t is the time, z is the distance along the adsorber, ρ is the framework density, ε is the bed voidage, v is the interstitial gas velocity, and $\bar{q}_i(t,z)$ is the *spatially averaged* molar loading within the crystallites of radius r_c, monitored at position z, and at time t. The $\bar{q}_i(t,z)$ is determined by combining Eq. (11) with the appropriate M–S model for the fluxes, Eqs. 5 and 6. In other words, the uptake calculations need to be performed at every position along the adsorber.

If the value of $Đ_i/r_c^2$ is large enough to ensure that intra-crystalline gradients are absent and the entire crystallite particle can be considered to be in thermodynamic equilibrium with the surrounding bulk gas phase at that time t, and position z of the adsorber

$$\bar{q}_i(t,z) = q_i(t,z) \tag{13}$$

The molar loadings at the *outer surface* of the crystallites, i.e., at $r = r_c$, are calculated on the basis of adsorption equilibrium with the bulk gas phase partial pressures p_i at that position z and time t. The adsorption equilibrium can be calculated on the basis of the

IAST. Typically, the assumption of thermodynamic equilibrium leads to "sharp" breakthroughs, as illustrated by a variety of examples in Fig. 7.

For any mixture separation, the influence of diffusion can be subdivided into four categories A, B, C, and D, as follows.

Category A: In this case, there is only minor influence of intra-crystalline diffusion on breakthrough characteristics. The hierarchy of breakthroughs, when compared to equilibrium simulations, is not affected.

Category B: Here we have a strong influence of intra-crystalline diffusion on breakthrough characteristics. The productivity or capture capacity is reduced due to diffusional influences. The hierarchy of breakthroughs, when compared to equilibrium simulations, is not affected, however.

Category C: Strong influence of intra-crystalline diffusion on breakthrough characteristics. The hierarchy of breakthroughs is altered; the components with lower diffusivities break through significantly earlier, when compared to equilibrium simulations.

Category D: Strong influence of intra-crystalline diffusion, and specifically thermodynamic coupling effects, on breakthrough characteristics. The productivity is enhanced by thermodynamic coupling effects.

Examples of separations in each of the four categories of materials are listed in Table 1. The Supplementary material contains detailed simulations for each of the listed separations. We discuss below some of the highlights of our analyses.

Fig. 7a presents experimentally determined breakthrough curves obtained for 50/50 CO_2/N_2 mixture using activated sample of Cu-TDPAT [66]. The continuous solid lines represent breakthrough simulations assuming thermodynamic equilibrium, i.e., invoking Eq. (13). The agreement between the two sets is reasonably good; it is particularly noteworthy that the breakthrough times are correctly captured in the simulations. It has also been demonstrated by Wu et al. [66] that inclusion of intra-crystalline diffusion effects, invoking the flux relations (6), leads to breakthroughs that are practically indistinguishable from those obtained using Eq. (13).

Similarly, the experimentally determined breakthrough characteristics of CO_2/CH_4 mixtures in MgMOF-74 [67], and CO_2/N_2 mixtures in NiMOF-74 [68] can be adequately modeled assuming thermodynamic equilibrium, and invoking Eq.(13).

Yang et al. [58] have presented experimental data or transient breakthrough of 40/60 CO_2/CH_4 mixtures through fixed bed adsorber packed with K-KFI zeolite. The experimental data are in good agreement with breakthrough simulations that assume thermodynamic equilibrium, invoking Eq. (13); see Fig. 7b.

Fig. 7c compares the experimental data (symbols) of Silva et al. [69] on the breakthrough characteristics of 3-component 35.5/47/17.5 $H_2/CO_2/CH_4$ mixture in an adsorber packed with CuBTC with simulations that assume thermodynamic equilibrium (continuous solid lines). The agreement between the two sets is very good. Silva et al. [69] also present a detailed model for breakthrough that include: intra-crystalline diffusion, axial dispersion in the fixed bed, along with a rigorous energy balance. Their simulation results (presented in Fig. 4a of their paper) are hardly distinguishable from our own simulations invoking Eq. (13). Equilibrium breakthrough simulations are particularly useful for screening adsorbents for H_2 purification [66,70–74]. In this context, it must be remarked that the Banu et al. [71] have employed a detailed model, including intra-particle diffusion and axial dispersion in the fixed beds, to simulate the breakthroughs of 5-component $H_2/CO_2/CO/CH_4/N_2$ mixtures with several materials; as demonstrated in the Supplementary material, simulations invoking Eq. (13) produce nearly the same results and conclusions.

The characteristics of the experimentally determined transient breakthrough of an equimolar C_3H_6/C_3H_8 mixture in an adsorber bed packed with FeMOF-74 (=Fe_2(dobdc) = CPO-27-Fe) [55], that has one-dimensional hexagonal-shaped channels of 11 Å size, can be essentially captured by equilibrium simulations ignoring diffusion; see Fig. 7d. It has been established that alkenes are more strongly bound (the attachment is side-on to the Fe(II) atoms [55]), when compared to the alkanes; consequently, the alkanes are eluted first.

Transient breakthroughs of C_2H_4/C_2H_6 and C_3H_6/C_3H_8 mixture in an adsorber bed packed with CoMOF-74 [75], a structural analog of FeMOF-74, show similar sharp, near-vertical, breakthroughs that are indicative of absence of diffusional limitations; see Fig. 7e. An important feature of the alkane/alkene separations with CuBTC, FeMOF-74, MgMOF-74 and CoMOF-74 is that the desired alkene product, required for production of polymer grade polyethene and polypropene, can only be recovered in the desorption phase. For such materials we need to operate with multiple beds involving five different steps; the alkene product of the desired purity is recovered in the final step by counter-current vacuum blowdown [76,77].

The experimental data of Yoon et al. [78] for transient breakthrough of C_3H_6/C_3H_8 mixtures in a packed bed of CuBTC crystallites are presented in Fig. 7f. The unsaturated propene molecules bind more strongly with the Cu atoms than the saturated C_3H_8. The transient breakthrough characteristics are reasonably well represented by breakthrough simulations in which intra-crystalline diffusion effects are considered to be negligible and Eq. (13) is invoked.

Similarly, the separation of Xe and Kr from process gases from nuclear plants using NiMOF-74 [79] can be adequately described using equilibrium simulations. The selective removal of C_2H_2 from hydrocarbon mixtures in fixed beds of FeMOF-74, MgMOF-74, and CoMOF-74 is properly modeled assuming thermodynamic equilibrium [3,55]. The separation of isobutene/isobutane mixtures is fixed beds of CuBTC [80] can be adequately described assuming thermodynamic equilibrium, i.e., invoking Eq. (13). For the above mentioned examples, further details are provided in the Supplementary material.

If the guest molecules are strongly constrained within the framework, the values of $Đ_i/r_c^2$ for guest molecules are such that intra-crystalline diffusion resistances lead to less-sharp, more "diffuse", breakthroughs. To illustrate this let us consider the separation of O_2/N_2 for production of purified O_2, required, for example, in medical applications [1,81]. Using LTA-5A, the O_2/N_2 separation essentially relies on the fact that the adsorption strength of N_2 is 3.6 times that of O_2. The diffusion selectivity is in favor of O_2, with $Đ_{O2}/Đ_{N2} = 2$. The cations within the framework do not block the window regions and diffusional limitations are adequately quantified by taking $Đ_{O2}/r_c^2 = 0.01\ s^{-1}$ [81–83]. The continuous solid lines in Fig. 8a are simulations that include diffusional effects invoking the flux relations (6), ignoring thermodynamic coupling effects. Inclusion of thermodynamic coupling effects leads to practically identically breakthrough characteristics; this is because the differences in the adsorption strengths of O_2 and N_2 in LTA-5A are small. Pure O_2 can be recovered in the early stages of the breakthrough. The dashed lines in Fig. 8a are breakthrough simulations in which diffusional influences are ignored, and thermodynamic equilibrium is assumed to prevail within the crystals, invoking Eq. (13). Diffusional influences serve to produce more diffuse breakthrough characteristics and, as a consequence, the production capacity for pure O_2 is reduced. As illustration, let us say we need to enrich O_2 from 21% feed mixture to yield 85% O_2 in product gas. In absence of diffusional limitations the 85% pure O_2 productivity of LTA-5A is 1.58 mol L^{-1}. Taking intra-crystalline diffusion into account has the effect of reducing the productivity to 0.43 mol L^{-1}.

Difffusional effects are of lesser importance for O_2/N_2 separations using LiX (with Si/Al = 1, referred to as LiLSX) [84], that has

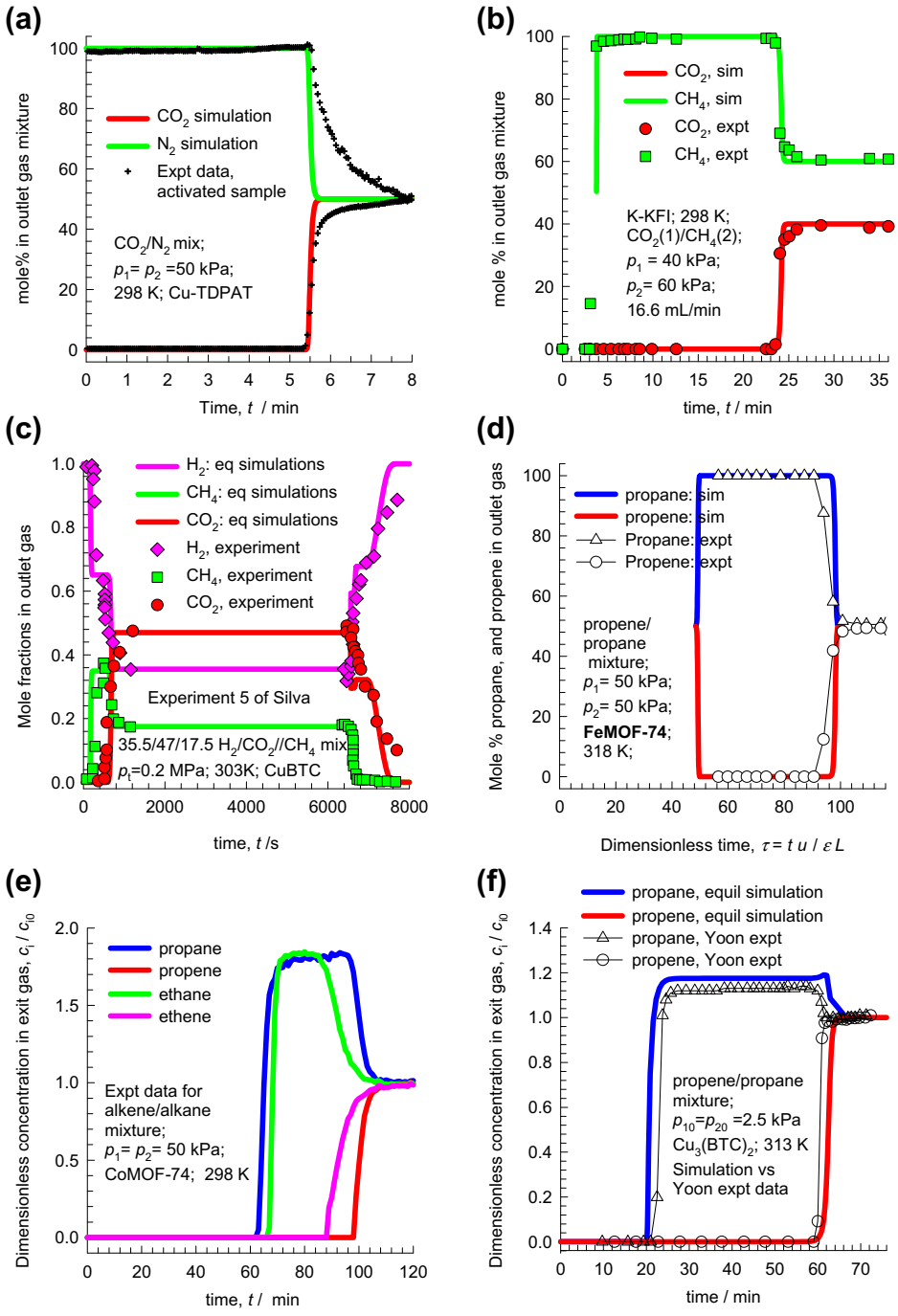

Fig. 7. (a) Experimentally determined breakthrough curves obtained for 50/50 CO_2/N_2 mixture using activated sample of Cu-TDPAT [66]. (b) Experimental data of Yang et al. [58] for transient breakthrough of 40/60 CO_2/CH_4 mixtures through fixed bed adsorber packed with K-KFI zeolite. (c) Adsorption/desorption breakthrough characteristics of 3-component 35.5/47/17.5 $H_2/CO_2/CH_4$ mixture in adsorber packed with CuBTC at 303 K operating at a total pressure of 0.2 MPa [69]. The desorption phase is initiated at time $t = 6550$ s; the 3-component mixture is switched to pure H_2. (d) Experimentally determined transient breakthrough of an equimolar C_3H_6/C_3H_8 mixture in an adsorber bed packed with FeMOF-74 [55]. (e) Experimental data on transient breakthrough of C_2H_4/C_2H_6 and C_3H_6/C_3H_8 mixtures in an adsorber bed packed with CoMOF-74 [75]. (f) Transient breakthrough of equimolar C_3H_6/C_3H_8 mixtures in packed bed adsorber with CuBTC crystallites [78]. The continuous solid lines represent breakthrough simulations assuming thermodynamic equilibrium, i.e., invoking Eq. (13). Further details are available in the Supplementary material.

wider 7.4 Å windows separating cages; cf. Fig. 8b. The breakthrough characteristics are less "diffuse", and breakthrough times are longer than is the case with LTA-5A; this leads to higher productivities of purified O_2 using LiLSX.

Tijsebaert et al. [85] have demonstrated the potential of RUB-41, an all-silica zeolite that has the RRO structural topology, for separation of cis-2-butene and trans-2-butene from 1-butene; this separation is of industrial importance because 1-butene is needed in the production of e.g., linear low density polyethylene (LLDPE). RUB-41 comprises a 2-dimensional intersecting channel system consisting of an 8-membered ring channel (0.27×0.5 nm) along [001], and a 10-membered ring channel (0.4×0.65 nm) along [100]. The measured data on adsorption indicates that the saturation capacities at adsorption equilibrium follow the hierarchy cis-2-butene > trans-2-butene $\gg$ 1-butene. This hierarchy is, we believe, ascribable to entropy effects dictated by molecule "footprints", such as that demonstrated for hexane isomer separation within 12-ring channels of AFI and MOR zeolites [86–88]. The

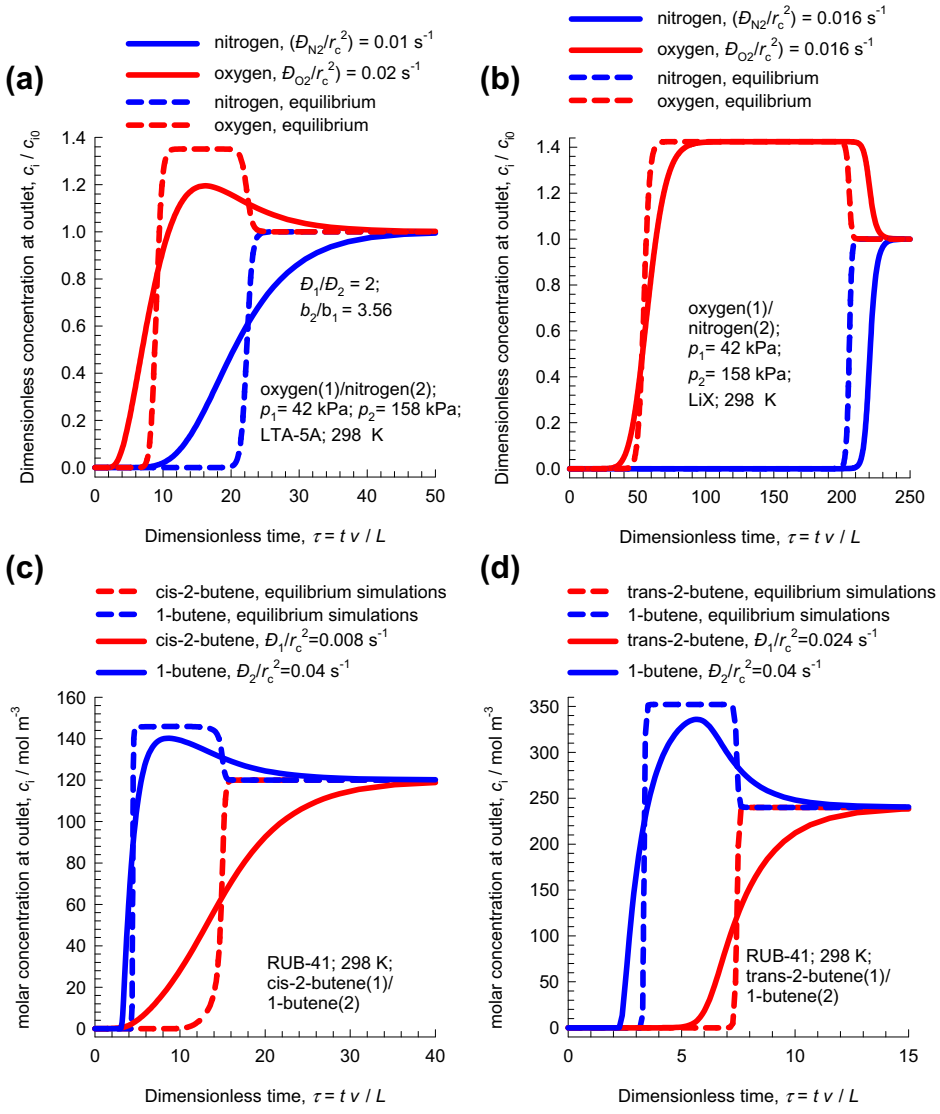

Fig. 8. (a, b) Influence of diffusional limitations on the breakthrough characteristics of O_2/N_2 mixture in a fixed bed adsorber packed with (a) LTA-5A, and (b) LiX. (c, d) Influence of diffusional limitations on the breakthrough characteristics of (c) cis-2-butene/1-butene, and (d) trans-2-butene/1-butene mixtures using RUB-41 zeolite, operating in the liquid phase. The dashed lines are equilibrium breakthrough simulations, i.e., invoking Eq. (13). The continuous solid lines represent breakthrough simulations including diffusional limitations, using uncoupled flux Eq. (6). Further details are available in the Supplementary material.

footprint of 1-butene is longer than that of either cis-2-butene or trans-2-butene. As a consequence it is possible to pack more molecules of either cis-2-butene or trans-2-butene within a given length of the 10-ring channels of RUB-41. Differences in molecular lengths provides the rationale for the hierarchy of saturation loadings that follows cis-2-butene > trans-2-butene $\gg$ 1-butene. Breakthrough experiments of Tijsebaert et al. [85], carried out in the liquid phase, indicate that 1-butene breaks through earlier than either cis-2-butene, or trans-2-butene. Using the fits of the pure component isotherms, the experimental breakthroughs can be reasonably well described by breakthrough simulations that include the influence of intra-crystalline diffusion. Fig. 8c and d demonstrate the influence of intra-crystalline diffusion on transient breakthroughs. The sequence of breakthroughs is unaltered when diffusional influences are accounted for.

The experimental data of Remy et al. [89] for breakthroughs for CO_2/CH_4 mixtures in K-KFI, and Na-KFI zeolites exemplify the diffuse breakthroughs that are characteristic of diffusional influences; see Fig. 9a and b. The continuous solid lines in (a) and (b) represent breakthrough simulations allowing for intra-crystalline diffusion using flux Eq. (6) that ignore both correlations and thermodynamic coupling. The simulations capture all the essential characteristics of the experimental breakthroughs. Since the values of the $Đ_i/r_c^2$ used in the breakthrough simulations are essentially "fitted" to just one data set, there is no real justification for adopting more rigorous M–S model Eq. (5), accounting for thermodynamic coupling. The CO_2 breakthroughs are predicted reasonably well by use of the flux Eq. (6). For CH_4, there are differences between the breakthrough times predicted by simulations and the experimental data; these differences are most likely due to delay times in the experimental data sets.

At first sight, the two sets of results presented in Fig. 9a, and Fig. 7b, appear to infer different conclusions with regards to the influence of intra-crystalline diffusion effects in K-KFI. However, these data sets can be rationalized as follows. In the experiments of Yang et al. [58] the size of the crystals packed into the breakthrough tube were in the 40–80 mesh range, corresponding to crystallite sizes in the range of 180–420 μm; this size range is lower than the size range of 500–650 μm that was used in the experiments of Remy et al. [89]. A larger crystallite size is indicative of a

stronger influence of intra-crystalline diffusion, since the diffusional influences scale with r_c^2. A further reason that thermodynamic equilibrium is a good assumption in the experiments of Yang et al. [58] is that the contact times in their experiments are significantly higher, as compared to the breakthrough experiments of Remy et al. [89]; this is evidenced by the fact that the breakthroughs of CO_2 occurs at a significant later time in Fig. 9a in comparison to the data in Fig. 7b. Longer contact times ensure that the component loadings within the crystals are closer to equilibrium conditions.

Further evidence that the influence of intra-crystalline diffusion could alter when the operating conditions are changed is provided by the experimental breakthrough data of Peter et al. [90] for CO_2/CH_4 mixtures in amino-MIL-53(Al). These data indicate that intra-crystalline diffusion becomes of importance for operations at 3 MPa, while operations at pressures lower than 0.5 MPa show no discernible influence of diffusion limitations; see breakthrough simulations presented in the Supplementary material.

Experimental data on breakthroughs of ethylbenzene/o-xylene/m-xylene/p-xylene mixtures using MIL-47 [91], MIL-53 [92], Zn(bdc)dabco [93], and NiMOF-74 [52] can be essentially captured by breakthrough simulations allowing for intra-crystalline diffusion. To illustrate this, Fig. 9c compares the transient breakthrough experiments of Peralta et al. [52] for m-xylene/p-xylene mixtures in NiMOF-74, with breakthrough simulations allowing for intra-crystalline diffusion using flux Eq. (6) that ignore both correlations and coupling. From a technological point of view, the above mentioned materials are not the best choices for xylene isomer separation because we desire MOFs that selectively adsorb p-xylene. Based on the evidence presented in the Supplementary material, it appears that Co(BDP) is better suited for this separation, but experimental confirmation is required.

In Fig. 9d, the experimental data of Gücüyener et al. [57] on transient breakthrough of $C_2H_4/C_2H_6/H_2$ mixtures in a fixed bed adsorber packed with ZIF-7 are compared with simulations that include intra-crystalline diffusion effects using flux Eq. (6); there is good agreement between the the two sets. Adsorption favors the saturated C_2H_6, and therefore the desired C_2H_4 product can be recovered during the adsorption phase. Gücüyener et al. [57] characterize the breakthrough characteristics of ZIF-7 as being "turned on its head", with attendant practical advantages over materials such as CuBTC, FeMOF-74, MgMOF-74, and CoMOF-74. The experimental data of Böhme et al. [75] for transient breakthrough of C_2H_4/C_2H_6, and C_3H_6/C_3H_8 mixtures demonstrate that it is also possible to recover pure alkene in the adsorption cycle using ZIF-8. It is also to be noted that the alkane diffusivity in ZIF-7 and ZIF-8 is expected to be lower than that of the corresponding alkenes, due to subtle differences in bond lengths and bond angles [30]; if the differences in the diffusivities are sufficiently large, then we should expect the alkanes to break through earlier [3]. We need MOFs that

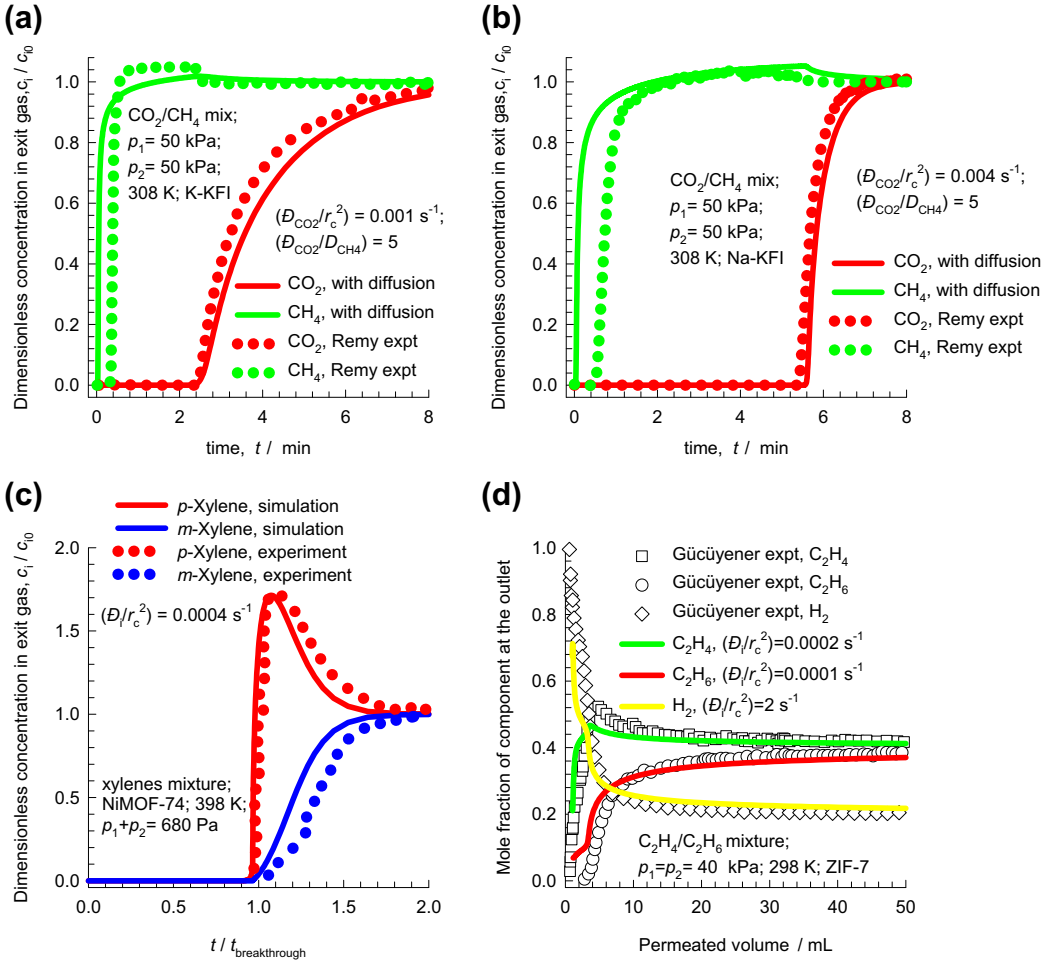

Fig. 9. (a, b) Experimental data on breakthrough of equimolar CO_2/CH_4 mixtures through a fixed bed adsorbers packed with (a) K-KFI, and (b) Na-KFI zeolite [89]. (c) Experimental breakthrough of m-xylene/p-xylene mixture in NiMOF-74 bed [52]. (d) Experimental data on transient breakthrough of $C_2H_4/C_2H_6/H_2$ mixtures in a fixed bed adsorber packed with ZIF-7 [57]. The continuous solid lines represent breakthrough simulations using flux Eq. (6). Further details on all the breakthrough simulations are available in the Supplementary material.

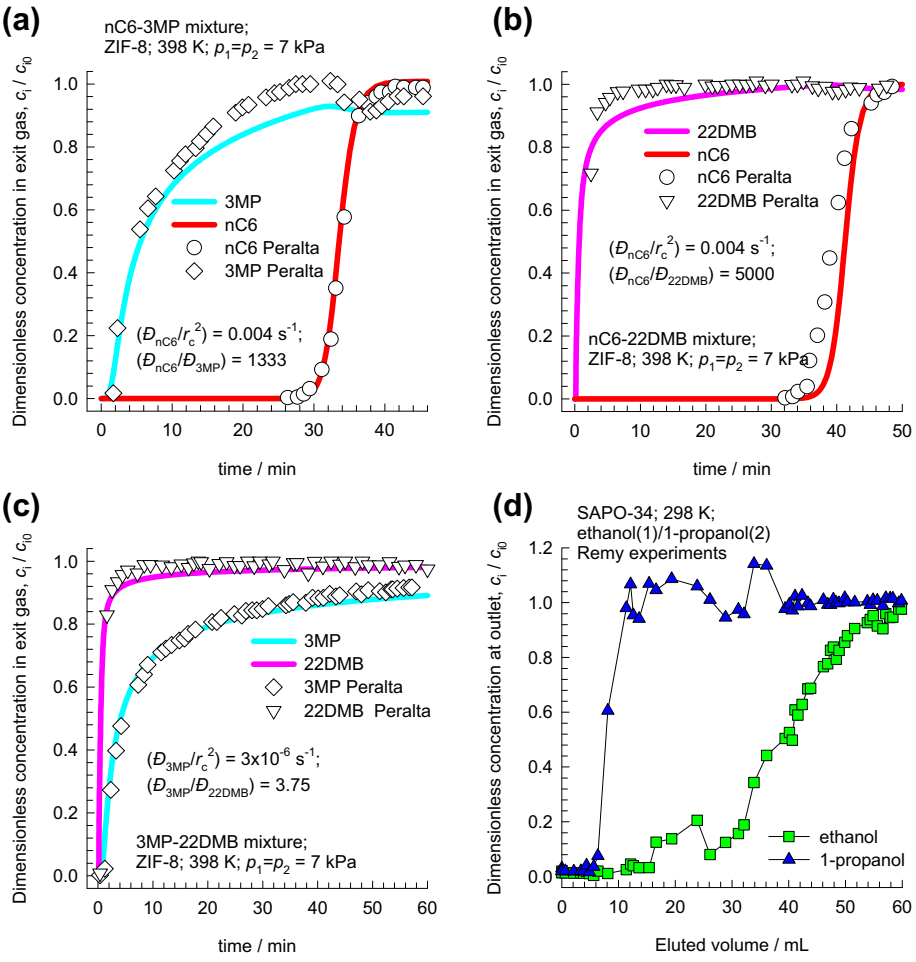

Fig. 10. (a, b, c) Experimental breakthrough (symbols) for (a) *n*C6/3MP, (b) *n*C6/22DMB, and (c) 3MP/22DMB mixtures in ZIF-8 [54] compared with simulations (continuous solid lines), using flux Eq. (6) ignoring thermodynamic coupling. (d) Breakthrough experimental data of Remy et al. [46] for separation of ethanol/1-propanol mixtures in a fixed bed adsorber packed with SAPO-34. Further details are available in the Supplementary material.

display adsorption selectivity towards the alkanes, but do not suffer from strong diffusion limitations; this is a fruitful area for further research.

For all the examples presented in Figs. 8 and 9, the introduction of diffusional resistances does not alter the hierarchy of breakthroughs and the diffusional influences are of a quantitative nature, often lowering the productivity.

Diffusional effects may also serve to enhance the separation performance in fixed bed adsorbers. This is illustrated in Fig. 10 by the experimental breakthrough data of Peralta et al. [54] for (a) *n*C6/3MP, (b) *n*C6/22DMB, and (c) 3MP/22DMB mixtures in ZIF-8. The three sets of breakthroughs can be adequately modeled by simulations using flux Eq. (6) with the diffusivity values of $Đ_{nC6}/r_c^2$ = 0.004 s^{-1}; $Đ_{3MP}/r_c^2 = 2 \times 10^{-6}$ s^{-1}; $Đ_{22DMB}/r_c^2 = 8 \times 10^{-7}$ s^{-1}.

For *n*C6/3MP separation, the ratio $Đ_{nC6}/Đ_{3MP}$ = 1333 ensures that 3MP breaks through significantly earlier than predicted on the basis of adsorption equilibrium, thereby improving separations; see Fig. 10a. Similarly, the separation of nC6/22DMB and 3MP/22DMB mixtures is improved by the significantly lower diffusivity of the hexane isomer with the higher degree of branching.

The breakthrough experimental data of Remy et al. [46] for separation of ethanol/1-propanol mixtures in a fixed bed adsorber packed with SAPO-34, shown in Fig. 10d, are quite remarkable because the component that is eluted first from the adsorber is the alcohol with the longer chain length. The rationalization of these experimental data can be traced to the entropy effects that favor the shorter alcohols under conditions such that the bulk fluid phase is in the liquid state [94]. When operating under conditions such that the bulk fluid phase is a liquid mixture, both adsorption and diffusion favor the uptake of the shorter alcohol, and the longer alcohol is rejected in a fixed bed adsorber. Breakthrough simulations taking proper account of adsorption, diffusion, and thermodynamic coupling are required to capture the experimentally observed behaviors; see Supplementary material.

In the extreme case, differences in diffusivities can serve to reverse the hierarchy of breakthroughs anticipated on the basis of mixture adsorption equilibrium. To illustrate this, consider the production of pure N_2 from O_2/N_2 mixtures using LTA-4A. Diffusion limitations are much more severe in LTA-4A, as compared to LTA-5A, because the window regions are partially blocked by the cations [4,15]. The production of pure N_2 relies on the significantly lower diffusivity of N_2 as compared to O_2. The continuous solid lines in Fig. 11a are simulations include diffusional effects with $Đ_{O2}/r_c^2 = 2 \times 10^{-3}$ s^{-1}; $Đ_{O2}/Đ_{N2}$ = 100 [95,96]. Pure N_2 can be recovered during the early stages of the breakthrough, albeit for a brief period. The dashed lines are breakthrough simulations in which diffusional influences are ignored, and thermodynamic equilibrium is assumed to prevail within the crystals. Introduction of strong diffusional limitations serves to reverse the hierarchy of breakthroughs, that is essential for N_2 production with LTA-4A.

A completely different strategy for N_2 production is to use Fe-MOF-74 as adsorbent; in this case O_2 binds selectively with the Fe atoms of the framework that consists of hexagonal-shaped one-dimensional channels of 11 Å size. The O_2 binding with Fe(II)

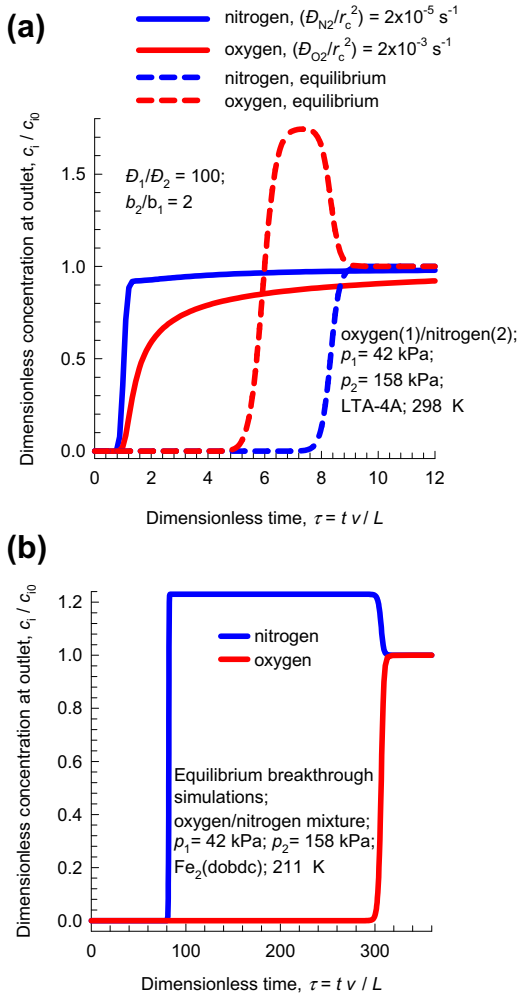

Fig. 11. (a) Influence of diffusional limitations on the breakthrough characteristics of $O_2(1)/N_2(2)$ mixture in a fixed bed adsorber packed with LTA-4A. The continuous solids lines are simulations include diffusional effects using uncoupled flux Eq. (6). The dashed lines are breakthrough simulations assuming thermodynamic equilibrium, i.e., invoking Eq. (13). (b) Simulations of the breakthrough characteristics of $O_2(1)/N_2(2)$ mixture in a fixed bed adsorber packed with FeMOF-74 operating at a total pressure of 100 kPa and 211 K [97]. Further details are available in the Supplementary material.

atoms has been demonstrated to be reversible up to temperatures of 211 K [97]. Diffusional influences are of negligible importance in FeMOF-74 and higher N_2 productivity is expected as compared to LTA-4A; this is evidenced by the breakthrough simulations in Fig. 11b that indicate significantly longer breakthrough times. Further experimental work is required to confirm the potential of FeMOF-74 for N_2 production.

6. Transient breakthrough of alkane isomers in MFI packed bed

The isomerization of alkanes, for the purposes of octane improvement, is a process of importance in the petroleum industry [47,54,56,98,99]. The product from the isomerization reactor, that commonly uses MOR zeolite as catalyst, consists of an equilibrium distribution of unreacted *n*-hexane (*n*C6), along with its mono-branched isomers 2-methylpentane (2MP), 3-methylpentane (3MP) and di-branched isomers 2,2-dimethylbutane (22DMB) and 2,3-dimethylbutane (23DMB). In current industrial practice the linear *n*C6 is separated from the branched isomers using LTA-5A in an adsorption separation step that relies on molecular sieving [98]. The 4.1 Å sized windows of LTA-5A only allow the diffusion and adsorption of the linear isomer, and the branched isomers are rejected and removed as higher-octane product. The unreacted *n*C6 is recycled back to the isomerization reactor.

The values of the Research Octane Number (RON) increases with the degree of branching; for hexane isomers, we note that the RON values are: *n*C6 = 30, 2MP = 74.5, 3MP = 75.5, 22DMB = 94, 23DMB = 105. Therefore, di-branched isomers are preferred products for incorporation into the high-octane gasoline pool. An improved process would require the recycle of both linear and mono-branched isomers to the reactor; see Fig. 12. The separation of 22DMB and 23DMB from the remaining isomers is a difficult task because it requires distinguishing molecules on the degree of branching. Typically, in such a processing scheme the aim would be to produce a product stream from the separation step with RON value higher than 92. This requirement of 92+ RON implies that the product stream will contain predominantly the di-branched isomers 22DMB and 23DMB, while allowing a small proportion of 2MP and 3MP to be incorporated into the product stream. Sharp separations between mono- and di-branched isomers is not a strict requirement, provided the 92+ RON requirement is met.

We shall now demonstrate that MFI zeolite has great potential for the use in the separation step in Fig. 12, because of the syner-

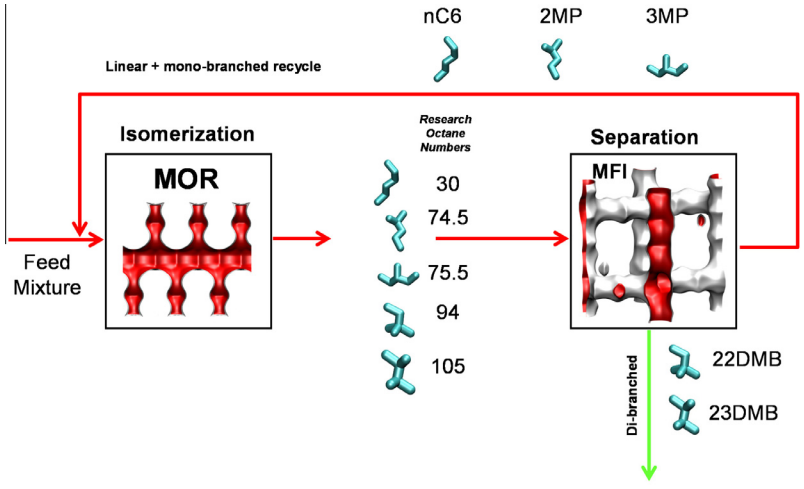

Fig. 12. Improved process for *n*C6 isomerization using MFI in the separation step.

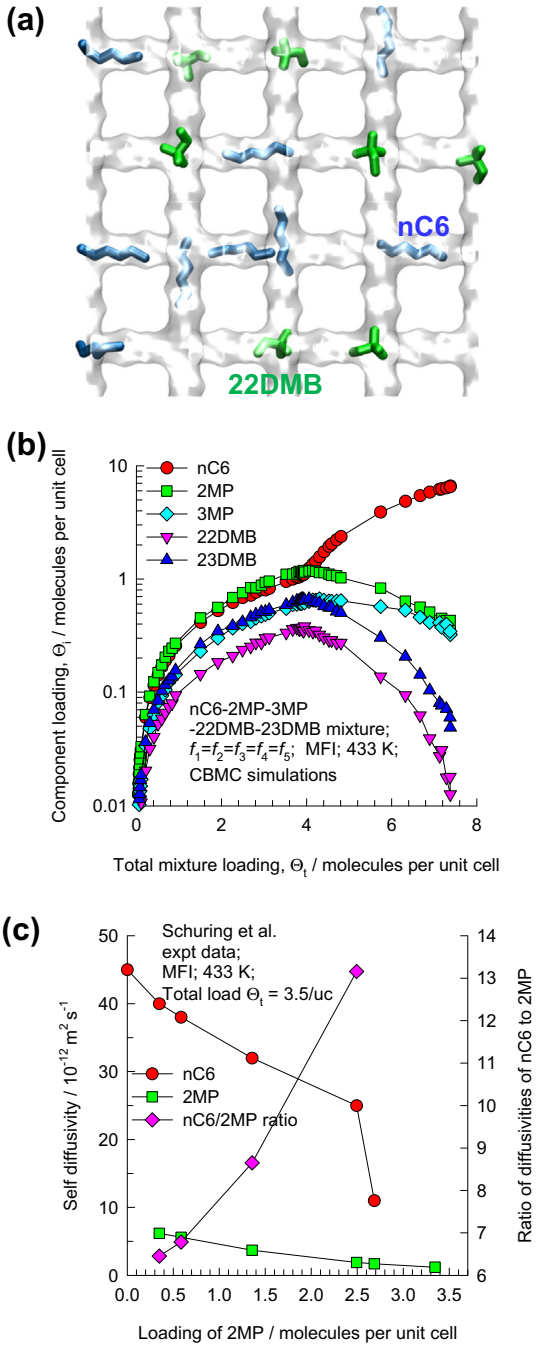

Fig. 13. (a) Snapshot showing the location of *n*C6 and 22DMB molecules within MFI. (b) CBMC simulations of component loadings in 5-component *n*C6/2MP/3MP/22DMB/23DMB mixture in MFI at 433 K. (c) Experimental data [104] on self-diffusivities of *n*C6 and 2-methylpentane (2MP) as a function of the loading of 2MP, keeping the total loading $\Theta_t = 3.5$/uc. Details of the CBMC simulation methodology, including detailed experimental validation, are available in the Supplementary material.

gistic effect of adsorption and intra-crystalline diffusion. Furthermore, we aim to show that thermodynamic coupling effects cannot be ignored for description of intra-crystalline diffusion, because such effects enhance the 92+ RON productivity. The separation of hexane isomers with MFI falls into the Category D listed in Table 1. The separation of CFC-115/HFC-125 mixtures with MFI has a similar character.

MFI appears in the list of materials patented by Universal Oil Products (UOP) for separation of hexane isomers [86,100–102].

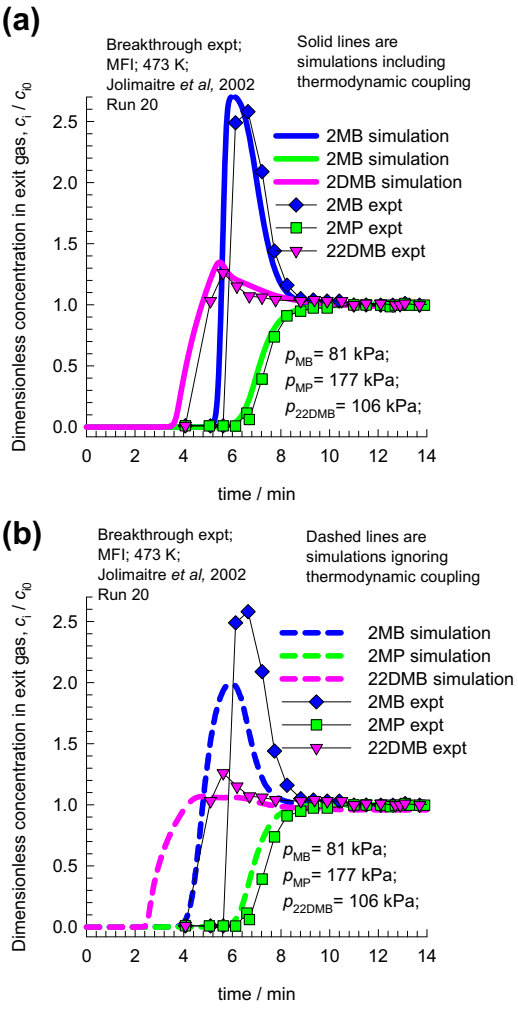

Fig. 14. Comparison of breakthrough experiments (Run 20) of Jolimaître et al. [106] for 2MB/2MP/22DMB ternary mixtures at 473 K with simulations. (a) The continuous solid lines are breakthrough calculations using Eq. (5) for fluxes and including thermodynamic coupling. (b) The dashed lines are the breakthrough simulations using flux Eq. (6), ignoring thermodynamic coupling. Further details are available in the Supplementary material, including breakthrough simulations for all of the Jolimaître experimental campaigns.

The separation relies essentially on configurational entropy effects; mono-branched and di-branched isomers prefer to locate at the intersections of MFI, because these are too bulky to locate within the channels [103]; Fig. 13a is a snapshot of the location of *n*C6 and 22DMB. There are 4 intersection sites per unit cell of MFI, and when the intersections are fully occupied, no more branched isomers can be adsorbed. Loadings $\Theta_t > 4$ per unit cell can only be realized by adsorption of the linear *n*C6, at the expense of the branched isomers. CBMC simulations of component loadings in *n*C6/2MP/3MP/22DMB/23DMB mixtures demonstrates that configurational entropy effects manifest at total mixture loadings $\Theta_t > 4$, causing the hierarchy to be *n*C6 > 2MP > 3MP > 23DMB > 22DMB; see Fig. 13b. Details of the CBMC simulation methodology, including detailed experimental validation, are available in the Supplementary material.

Schuring et al. [104] have reported experimental data on the self-diffusivities of both *n*C6 and 2MP in in C6/2MP mixtures; see Fig. 13c. The data show that *both* self-diffusivities are reduced with increasing loading of 2MP in the mixture. The preferential location of 2MP at the intersections causes blocking of molecular traffic in the intersecting channel system of MFI. MD simulations show that such intersection blocking effects also manifest in *n*C6/22DMB

mixtures [105]. We also note that the linear nC6 has a diffusivity that is about an order of magnitude higher than that of the branched 2MP. The right axis of Fig. 13c presents the data on the ratio of the self-diffusivities. With increased 2MP loading, the ratio of diffusivities of *n*C6–2MP increases. This implies that there are no slowing-down effects of *n*C6 due to the presence of the tardier 2MP. Rather, there is a relative enhancement of the mobility of *n*C6 with respect to 2MP with increased loading. Put another way, when analysing mixture diffusion of hexane isomer mixtures correlation effects can be ignored as a conservative estimate. The diffusion of *n*C6/2MP mixture in MFI has very special and unusual characteristics; *n*C6 is much more mobile, by about one order of magnitude. Furthermore, as a consequence of configurational entropy effects, the more strongly adsorbed species is also *n*C6. We therefore have a mixture of more-mobile-more-strongly-adsorbed-*n*C6 and tardier-less-strongly-adsorbed-2MP. There is uncommon synergy between adsorption and diffusion of alkane isomers in MFI zeolite.

The key separation in the process scheme presented in Fig. 12 is that between the mono-branched and di-branched isomers. We first seek experimental verification that this separation can be achieved in a fixed bed filled with MFI zeolite. For this purpose, we analyzed, and simulated, a set of experimental breakthrough experiments reported by Jolimaître et al. [106] for binary and ternary mixtures containing 2-methylbutane (2MB), 2MP, and 22DMB mixtures. Seven different experimental campaigns of Jolimaître with wide variation in the inlet partial pressures could be simulated with very good accuracy assuming the values $Đ_{2MB}/r_c^2 = 0.0075\ s^{-1}$; $Đ_{2MP}/r_c^2 = 0.005\ s^{-1}$; $Đ_{22DMB}/r_c^2 = 0.0000625\ s^{-1}$ for each of of seven experimental runs. As illustration, Fig. 14a compares the experimental breakthroughs in Run 20 for 2MB/2MP/22DMB ternary mixtures with breakthrough calculations using Eq. (5) for fluxes that takes account of thermodynamic coupling. The inclusion of thermodynamic coupling is vital; if thermodynamic coupling is ignored (i.e., using flux Eq. (6)) the agreement between the experiment and simulations is significantly poorer; see dashed lines Fig. 14b. The same conclusion is valid for each of the seven experimental campaigns; the evidence is contained in the Supplementary material.

Having established the potency of our breakthrough simulation methodology for alkane isomer separations with MFI, we proceed further to determine the 92+ RON productivity of MFI for separa-

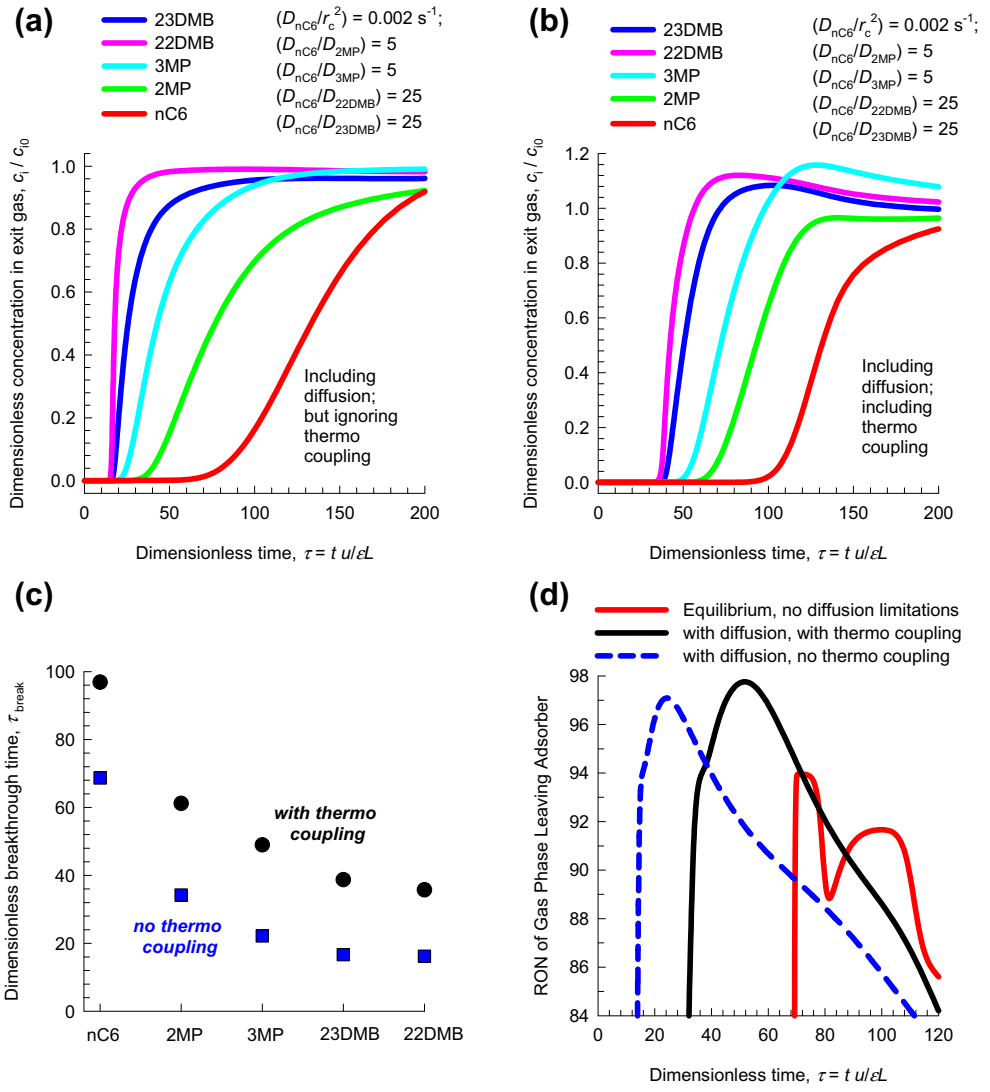

Fig. 15. Breakthrough characteristics 5-component nC6/2MP/3MP/22DMB/23DMB mixture in a fixed bed adsorber packed with MFI operating at a total pressure of 100 kPa and 433 K. (a) Breakthrough simulations using flux Eq. (6), ignoring thermodynamic coupling. (b) Simulations using flux Eq. (5) that includes thermodynamic coupling. (c) Comparison of dimensionless breakthrough times for each hexane isomer. (d) Influence of diffusional limitations on the RON of product gas exiting the MFI adsorber. Further details are available in the Supplementary material.

tion of an equimolar 5-component *n*C6/2MP/3MP/22DMB/23DMB mixture of hexane isomers in a fixed bed adsorber. For an operating temperature of 433 K, and total pressure of 100 kPa, the breakthrough simulations are presented in Fig. 15a, and b for two different scenarios: (a) ignoring thermodynamic coupling (i.e., using flux Eq. (6)) and (b) including thermodynamic coupling (i.e., using flux Eq. (5)). For both scenarios, the sequence of breakthroughs is 22DMB, 23DMB, 3MP, 2MP, and nC6; this hierarchy is dictated by a combination of two factors: (a) hierarchy of component loadings in the CBMC mixture simulations (cf. Fig. 13b) and (b) the diffusivities of the isomers that are chosen to be $Đ_{nC6}/r_c^2 = 0.002\ s^{-1}$; $Đ_{nC6}/Đ_{2MP} = 5$; $Đ_{nC6}/Đ_{3MP} = 5$; $Đ_{nC6}/Đ_{22DMB} = 25$; $Đ_{nC6}/Đ_{23DMB} = 25$. The considerations leading to this choice of the diffusivities are provided in the Supplementary material. For both scenarios, the high RON products 22DMB and 23DMB are recovered in the earlier stages of the breakthrough. Inclusion of thermodynamic coupling causes the breakthroughs of all isomers to be delayed. Fig. 15c compares the dimensionless breakthrough times, τ_{break} of each isomer for the two different scenarios; here τ_{break} is defined as the time at which the composition of the isomer at the outlet exceeds 1% of the value at the inlet, i.e., $(c_i/c_{i0}) > 0.01$. The differences in the breakthrough times for the mono-branched 3MP and di-branched isomer 23DMB is crucial for producing high RON product gas. If we ignore thermodynamic coupling, the values of τ_{break} for 3MP and 23DMB are 22.2 and 16.7, respectively. If we take proper account of thermodynamic coupling the corresponding values of τ_{break} for 3MP and 23DMB are 49 and 38.8. Consequently, inclusion of thermodynamic coupling has the effect of widening the gap between the breakthroughs of 3MP and 23DMB; this widening is beneficial for the producing high RON product. Fig. 15d presents calculations of the RON of the product gas exiting from the MFI adsorber. Three different breakthrough calculation scenarios are used in the calculations of the product RON: (a) equilibrium simulations, invoking Eq. (13) (b) using flux Eq. (6), ignoring thermodynamic coupling, and (c) use flux Eq. (5) that includes thermodynamic coupling. Introduction of diffusional influences leads to earlier breakthroughs of the di-branched isomers with respect to the mono-branched isomers, leading to higher RON values for earlier times. Inclusion of thermodynamic coupling in the flux equations, leads to higher RON product in the later stages of the breakthrough. From a material balance the productivity of MFI for producing 92+ RON product, expressed per L of crystalline material, are: (a) 0.205 mol L^{-1}, (b) 0.51 mol L^{-1}, and (c) 0.64 mol L^{-1}. Remarkably, the use of the rigorous M–S model including thermodynamic coupling effects results in significantly higher 92+ RON productivity. This is a clear demonstration of the beneficial effect of the synergy between adsorption and diffusion in MFI zeolite.

We now compare the performance of MFI with that ZIF-77 and $Fe_2(BDP)_3$ that have emerged as the "best" adsorbent for separation of hexane isomers in the recent comprehensive studies of Dubbeldam et al. [99] and Herm et al. [56], respectively. Fig. 16 presents a plot of 92+ RON productivities obtained with assumption of thermodynamic equilibrium (*x*-axis) versus that obtained with inclusion of diffusion limitations (*y*-axis) for MFI, $Fe_2(BDP)_3$, and ZIF-77. The inclusion of diffusional influences is beneficial for the 92+ RON productivity of MFI. For both $Fe_2(BDP)_3$, and ZIF-77, inclusion of intra-crystalline diffusion results in a severe reduction in 92+ RON productivity. When thermodynamic coupling effects are properly accounted for by use of flux Eq. (5), the 92+ RON productivity is significantly higher than either $Fe_2(BDP)_3$, or ZIF-77. The 92+ RON productivity of MFI is also higher than that obtained with several other materials such as ZIF-8 [54], BEA [107], Zn(bdc)dabco [108], ZnHBDC [109], UiO-66 [110], CFI [111] and ATS [112], that have been suggested in the literature for this separation task; further details are provided in the Supplementary material.

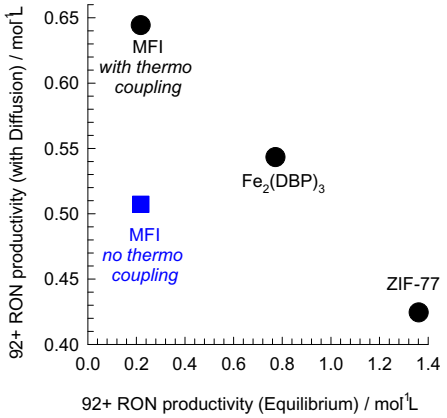

Fig. 16. Comparison of 92+ RON productivities of ZIF-77, $Fe_2(BDP)_3$, and MFI for separation of hexane isomers. The productivity values plotted on the *x*-axis are obtained from breakthrough simulations with assumption of thermodynamic equilibrium i.e., invoking Eq. (13). The productivity values on the *y*-axis are obtained from breakthrough simulations taking intra-crystalline diffusion into account. For MFI, the productivity values are obtained using both flux Eq. (6), ignoring thermodynamic coupling, and Eq. (5) that includes thermodynamic coupling. Further details are available in the Supplementary material.

7. Conclusions

The main objective of this article was to underscore the need to adopt the Maxwell–Stefan formulation for modeling intra-crystalline diffusion in ordered nanoporous materials. The M–S formulation clearly differentiates between two types of coupling: (a) coupling due to correlation effects, modeled by the exchange coefficient $Đ_{12}$, and (b) thermodynamic coupling effects quantified by sizable off-diagonal elements of $[\Gamma]$. The major conclusions of this article are summarized below.

(1) Correlation effects need to be properly modeled for mixtures of more-mobile-less-strongly-adsorbed and tardier-more-strongly-adsorbed species as exemplified by permeation of H_2/CO_2 CH_4/C_2H_6, CH_4/C_3H_8 mixtures across MFI membranes. Correlation effects generally cause the slowing-down of the more mobile partner species.
(2) Generally speaking, correlation effects are of negligible importance when modeling permeation of mixtures across structures such as ZIF-8, SAPO-34, DDR, and LTA that consist of cages separated by narrow windows in the 3.4–4.1 Å range. Molecules hop one-at-a-time across the windows, and are largely uncorrelated.
(3) For transient mixture permeation, thermodynamic coupling effects can lead to maxima in the fluxes of the more mobile partner species in early stages of the transience.
(4) For transient uptake of binary mixtures within a nanoporous crystal, overshoots in the uptake of the more mobile partner species is traceable to the influence of thermodynamic coupling effects, quantified by sizable off-diagonal elements of $[\Gamma]$.
(5) Generally speaking, simulations of breakthroughs of mixtures in fixed-bed adsorbers assuming thermodynamic equilibrium and invoking Eq. (13) lead to sharp breakthroughs. Equilibrium simulations are adequate for modeling breakthroughs when the guest molecules are weakly confined within the pores of the framework.
(6) Intra-crystalline diffusion effects lead to more "diffuse", non-sharp, breakthrough characteristics in fixed bed adsorbers.
(7) Intra-crystalline diffusion effects can enhance separations in fixed beds; this is exemplified by *n*C6/3MP, *n*C6/22DMB, and 3MP/22DMB separations with ZIF-8.

(8) For separation of ethanol/1-propanol and ethanol/1-hexagonal mixtures with SAPO-34, there is unusually strong synergy between adsorption and diffusion.
(9) By appropriate choice of the host material, we can exploit differences in the diffusivities to reverse the hierarchy of breakthroughs. This strategy is adopted to obtain pure N_2 from O_2/N_2 feed mixtures with LTA-4A.
(10) Use of the simplified M–S flux Eq. (6), ignoring thermodynamic coupling, is adequate to model most breakthrough experiments. Exceptional circumstances prevail for the separation of hexane isomers using MFI zeolite; in this case the inclusion of thermodynamic coupling is important and has a beneficial effect on the separations. Due to synergy between adsorption and diffusion, MFI has the best productivity in separation of hexane isomers for octane enhancement.

Acknowledgement

Dr. Jasper M. van Baten is gratefully acknowledged for his assistance with the molecular simulations.

Appendix A. Supplementary data

Supplementary data associated with this article can be found, in the online version, at http://dx.doi.org/10.1016/j.micromeso.2013.10.026.

References

[1] D.M. Ruthven, S. Farooq, K.S. Knaebel, Pressure Swing Adsorption, VCH Publishers, New York, 1994.
[2] R. Krishna, R. Baur, Sep. Purif. Technol. 33 (2003) 213–254.
[3] Y. He, R. Krishna, B. Chen, Energy Environ. Sci. 5 (2012) 9107–9120.
[4] R. Krishna, J. Phys. Chem. C 113 (2009) 19756–19781.
[5] R. Krishna, Chem. Soc. Rev. 41 (2012) 3099–3118.
[6] R. Krishna, J.M. van Baten, Chem. Eng. Sci. 63 (2008) 3120–3140.
[7] R. Krishna, J.M. van Baten, Microporous Mesoporous Mater. 109 (2008) 91–108.
[8] A.L. Myers, J.M. Prausnitz, A.I.Ch.E.J. 11 (1965) 121–130.
[9] R. Krishna, J.M. van Baten, J. Membr. Sci. 430 (2013) 113–128.
[10] R. Krishna, J.M. van Baten, Chem. Eng. Sci. 64 (2009) 3159–3178.
[11] R. Krishna, J.M. van Baten, J. Membr. Sci. 377 (2011) 249–260.
[12] R. Krishna, J.M. van Baten, J. Membr. Sci. 383 (2011) 289–300.
[13] R. Krishna, J.M. van Baten, J. Phys. Chem. C 114 (2010) 11557–11563.
[14] R. Krishna, J.M. van Baten, Ind. Eng. Chem. Res. 45 (2006) 2084–2093.
[15] R. Krishna, J.M. van Baten, Microporous Mesoporous Mater. 137 (2011) 83–91.
[16] C. Chmelik, H. Bux, J. Caro, L. Heinke, F. Hibbe, T. Titze, J. Kärger, Phys. Rev. Lett. 104 (2010) 085902.
[17] A.I. Skoulidas, D.S. Sholl, R. Krishna, Langmuir 19 (2003) 7977–7988.
[18] S. Chempath, R. Krishna, R.Q. Snurr, J. Phys. Chem. B 108 (2004) 13481–13491.
[19] L. Sandström, E. Sjöberg, J. Hedlund, J. Membr. Sci. 380 (2011) 232–240.
[20] J.M. van de Graaf, F. Kapteijn, J.A. Moulijn, A.I.Ch.E.J. 45 (1999) 497–511.
[21] C.D. Baertsch, H.H. Funke, J.L. Falconer, R.D. Noble, J. Phys. Chem. 100 (1996) 7676–7679.
[22] B.H. Jeong, Y. Hasegawa, K. Kusakabe, S. Morooka, Sci. Technol. 37 (2002) 1225–1239.
[23] R. Krishna, J.M. van Baten, Phys. Chem. Chem. Phys. 15 (2013) 7994–8016.
[24] S. Li, J.L. Falconer, R.D. Noble, R. Krishna, Ind. Eng. Chem. Res. 46 (2007) 3904–3911.
[25] S. Li, J.L. Falconer, R.D. Noble, R. Krishna, J. Phys. Chem. C 111 (2007) 5075–5082.
[26] R. Krishna, S. Li, J.M. van Baten, J.L. Falconer, R.D. Noble, Sep. Purif. Technol. 60 (2008) 230–236.
[27] H. Bux, C. Chmelik, R. Krishna, J. Caro, J. Membr. Sci. 369 (2011) 284–289.
[28] Y. Pan, T. Li, G. Lestari, Z. Lai, J. Membr. Sci. 390–391 (2012) 93–98.
[29] D. Liu, X. Ma, H. Xi, Y.S. Lin, J. Membr. Sci. 451 (2014) 85–93.
[30] R. Krishna, J.M. van Baten, J. Phys. Chem. C 116 (2012) 23556–23568.
[31] K. Li, D.H. Olson, J. Seidel, T.J. Emge, H. Gong, H. Zeng, J. Li, J. Am. Chem. Soc. 131 (2009) 10368–10369.
[32] D.M. Ruthven, S.C. Reyes, Microporous Mesoporous Mater. 104 (2007) 59–66.
[33] E.R. Geus, H. van Bekkum, W.J.W. Bakker, J.A. Moulijn, Microporous Mater. 1 (1993) 131–147.
[34] T. Matsufuji, K. Watanabe, N. Nishiyama, Y. Egashira, M. Matsukata, K. Ueyama, Ind. Eng. Chem. Res. 39 (2000) 2434–2438.
[35] T. Matsufuji, N. Nishiyama, M. Matsukata, K. Ueyama, J. Membr. Sci. 178 (2000) 25–34.
[36] R. Kolvenbach, N. Al-Yassir, S.S.S.S. Al-Khattaf, O.C. Gobin, J.H. Ahn, A. Jentys, J.A. Lercher, Catal. Today 168 (2011) 147–157.
[37] L. Courthial, A. Bandot, M. Tayakout-Fayolle, C. Jallut, A.I.Ch.E.J. 59 (2013) 959–970.
[38] S.J. Bhadra, S. Farooq, Ind. Eng. Chem. Res. 50 (2011) 14030–14045.
[39] B. Majumdar, S.J. Bhadra, R.P. Marathe, S. Farooq, Ind. Eng. Chem. Res. 50 (2011) 3021–3034.
[40] H.W. Habgood, Canad. J. Chem. 36 (1958) 1384–1397.
[41] W. Niessen, H.G. Karge, Microporous Mater. 1 (1993) 1–8.
[42] H.G. Karge, C.R. Chim. 8 (2005) 303–319.
[43] N.W. Carlson, J.S. Dranoff, Competitive adsorption of methane and ethane on 4A zeolite, A.I. Liapis, Fundamentals of Adsorption, AIChE, New York, 1986.
[44] J. Kärger, M. Bülow, Chem. Eng. Sci. 30 (1975) 893–896.
[45] J.C. Saint-Remi, G.V. Baron, J.F.M. Denayer, J. Phys. Chem. C 117 (2013) 9758–9765.
[46] T. Remy, J.C. Saint-Remi, R. Singh, P.A. Webley, G.V. Baron, J.F.M. Denayer, J. Phys. Chem. C 115 (2011) 8117–8125.
[47] R. Krishna, Chem. Eng. Res. Des. 79 (2001) 182–194.
[48] R. Krishna, B. Smit, T.J.H. Vlugt, J. Phys. Chem. A 102 (1998) 7727–7730.
[49] G.D. Pirngruber, V. Carlier, D. Leinekugel-le-Cocq, Oil Gas Sci. Technol. (2013) (http://dx.doi.org/10.2516/ogst/2012067).
[50] G.D. Pirngruber, L. Hamon, S. Bourelly, P.L. Llewellyn, E. Lenoir, V. Guillerm, C. Serre, T. Devic, ChemSusChem 5 (2012) 762–776.
[51] L. Hamon, E. Jolimaître, G.D. Pirngruber, Ind. Eng. Chem. Res. 49 (2010) 7497–7503.
[52] D. Peralta, K. Barthelet, J. Pérez-Pellitero, C. Chizallet, G. Chaplais, A. Simon-Masseron, G.D. Pirngruber, J. Phys. Chem. C 116 (2012) (1855) 21844–21855.
[53] D. Peralta, G. Chaplais, A. Simon-Masseron, K. Barthelet, C. Chizallet, A.-A. Quoineaud, G.D. Pirngruber, J. Am. Chem. Soc. 134 (2012) 8115–8126.
[54] D. Peralta, G. Chaplais, A. Simon-Masseron, K. Barthelet, G.D. Pirngruber, Ind. Eng. Chem. Res. 51 (2012) 4692–4702.
[55] E.D. Bloch, W.L. Queen, R. Krishna, J.M. Zadrozny, C.M. Brown, J.R. Long, Science 335 (2012) 1606–1610.
[56] Z.R. Herm, B.M. Wiers, J.M. Van Baten, M.R. Hudson, P. Zajdel, C.M. Brown, N. Maschiocchi, R. Krishna, J.R. Long, Science 340 (2013) 960–964.
[57] C. Gücüyener, J. van den Bergh, J. Gascon, F. Kapteijn, J. Am. Chem. Soc. 132 (2010) 17704–17706.
[58] J. Yang, R. Krishna, J. Li, J. Li, Microporous Mesoporous Mater. 184 (2014) 21–27.
[59] M. Palomino, A. Corma, F. Rey, S. Valencia, Langmuir 26 (2010) 1910–1917.
[60] R. Krishna, J.R. Long, J. Phys. Chem. C 115 (2011) 12941–12950.
[61] D.M. Ruthven, Principles of Adsorption and Adsorption Processes, John Wiley, New York, 1984.
[62] R.T. Yang, Gas Separation by Adsorption Processes, Butterworth, Boston, 1987.
[63] D.D. Do, Adsorption Analysis: Equilibria and Kinetics, Imperial College Press, London, 1998.
[64] L.J.P. van den Broeke, R. Krishna, Chem. Eng. Sci. 50 (1995) 2507–2522.
[65] K.S. Walton, M.D. LeVan, Ind. Eng. Chem. Res. 42 (2003) 6938–6948.
[66] H. Wu, K. Yao, Y. Zhu, B. Li, Z. Shi, R. Krishna, J. Li, J. Phys. Chem. C 116 (2012) 16609–16618.
[67] T. Remy, S.A. Peter, S. Van der Perre, P. Valvekens, D.E. De Vos, G.V. Baron, J.F.M. Denayer, J. Phys. Chem. C 117 (2013) 9301–9310.
[68] J. Liu, J. Tian, P.K. Thallapally, B.P. McGrail, J. Phys. Chem. C 116 (2012) 9575–9581.
[69] B. Silva, I. Salomon, A.M. Ribeiro, J.S. Chang, J.M. Loureiro, A.E. Rodrigues, Sep. Purif. Technol. 118 (2013) 744–756.
[70] Z.R. Herm, R. Krishna, J.R. Long, Microporous Mesoporous Mater. 151 (2012) 481–487.
[71] A.M. Banu, D. Friedrich, S. Brandani, T. Düren, Ind. Eng. Chem. Res. 52 (2013) 9946–9957.
[72] G.Q. Kong, Z.D. Han, Y. He, S. Qu, W. Zhou, T. Yildirim, R. Krishna, C. Zou, C.D. Wu, B. Chen, Chem. Eur. J. 19 (2013) 14886–14894.
[73] Y. He, H. Furukawa, C. Wu, M. O'Keefe, R. Krishna, B. Chen, Chem. Commun. 49 (2013) 6773–6775.
[74] Y. He, S. Xiang, Z. Zhang, S. Xiong, C. Wu, W. Zhou, T. Yildirim, R. Krishna, B. Chen, J. Mater. Chem. A 1 (2013) 2543–2551.
[75] U. Böhme, B. Barth, C. Paula, A. Kuhnt, W. Schwieger, A. Alexander Mundstock, J. Caro, M. Hartmann, Langmuir 29 (2013) 8592–8600.
[76] F.A. Da Silva, A.E. Rodrigues, A.I.Ch.E.J. 47 (2001) 341–357.
[77] C.A. Grande, F. Poplow, A.E. Rodrigues, Sci. Technol. 45 (2010) 1252–1259.
[78] J.W. Yoon, I.T. Jang, K.-Y. Lee, Y.K. Hwang, J.-S. Chang, Bull. Korean Chem. Soc. 31 (2010) 220–223.
[79] J. Liu, P.K. Thallapally, D. Strachan, Langmuir 28 (2012) 11584–11589.
[80] M. Hartmann, S. Kunz, D. Himsl, O. Tangermann, S. Ernst, A. Wagener, Langmuir 24 (2008) 8634–8642.
[81] S. Farooq, D.M. Ruthven, H.A. Boniface, Chem. Eng. Sci. 44 (1989) 2809–2816.
[82] V. Rama Rao, S. Farooq, W.B. Krantz, A.I.Ch.E.J. 56 (2010) 354–370.
[83] V. Rama Rao, Adsorption based portable oxygen concentrator for personal medical applications, Ph.D. Thesis, Ph.D. Dissertation, National University of Singapore, Singapore, 2011.

[84] S.U. Rege, R.T. Yang, Ind. Eng. Chem. Res. 36 (1997) 5358–5365.
[85] B. Tijsebaert, C. Varszegi, H. Gies, F.S. Xiao, X. Bao, T. Tatsumi, U. Müller, D. De Vos, Chem. Commun. (2008) 2480–2482.
[86] R. Krishna, B. Smit, S. Calero, Chem. Soc. Rev. 31 (2002) 185–194.
[87] R. Krishna, J.M. van Baten, Sep. Purif. Technol. 55 (2007) 246–255.
[88] J.M. van Baten, R. Krishna, Microporous Mesoporous Mater. 84 (2005) 179–191.
[89] T. Remy, S.A. Peter, V. Van Tendeloo, S. Van der Perre, Y. Lorgouilloux, C.E.A. Kirschhock, G.V. Baron, J.F.M. Denayer, Langmuir 29 (2013) 4998–5012.
[90] S.A. Peter, G.V. Baron, J. Gascon, F. Kapteijn, J.F.M. Denayer, Adsorption (2013) (http://dx.doi.org/10.1007/s10450-013-9564-x).
[91] V. Finsy, H. Verelst, L. Alaerts, D. De Vos, P.A. Jacobs, G.V. Baron, J.F.M. Denayer, J. Am. Chem. Soc. 130 (2008) 7110–7118.
[92] T. Remy, G.V. Baron, J.F.M. Denayer, Langmuir 27 (2011) 13064–13071.
[93] M.P.M. Nicolau, P.S. Bárcia, J.M. Gallegos, J.A.C. Silva, A.E. Rodrigues, B. Chen, J. Phys. Chem. C 113 (2009) 13173–13179.
[94] R. Krishna, J.M. van Baten, Sep. Purif. Technol. 76 (2011) 325–330.
[95] S. Farooq, M.N. Rathor, K. Hidajat, Chem. Eng. Sci. 48 (1993) 4129–4141.
[96] S. Farooq, Gas Sep. Purif. 9 (1995) 205–212.
[97] E.D. Bloch, L. Murray, W.L. Queen, S.M. Chavan, S.N. Maximoff, J.P. Bigi, R. Krishna, V.K. Peterson, F. Grandjean, G.J. Long, B. Smit, S. Bordiga, C.M. Brown, J.R. Long, J. Am. Chem. Soc. 133 (2011) 14814–14822.
[98] W. Vermeiren, J.-P. Gilson, Top Catal 52 (2009) 1131–1161.
[99] D. Dubbeldam, R. Krishna, S. Calero, A.ö. Yazaydın, Angew. Chem., Int. Ed. 51 (2012) (1871) 11867–11871.
[100] H.W. Dandekar, G.A. Funk, R.D. Gillespie, H.A. Zinnen, C.P. McGonegal, M. Kojima, S.H. Hobbs, Process for alkane isomerization using reactive chromatography, UOP, Des Plaines, Illinois, USA., US 5763730, U.S., 1999.
[101] H.W. Dandekar, G.A. Funk, H.A. Zinnen, Process for separating and recovering multimethyl-branched alkanes, UOP LLC, Des Plaines, Illinois, USA., US 6069289, U.S., 2000.
[102] R.W. Carr, H.W. Dandekar, Adsorption with reaction, S. Kulprathipanja, Reactive Separation Processes, Taylor & Francis, New York, USA, 2001.
[103] R. Krishna, J.M. van Baten, Phys. Chem. Chem. Phys. 13 (2011) 10593–10616.
[104] D. Schuring, A.P.J. Jansen, R.A. van Santen, J. Phys. Chem. B 104 (2000) 941–948.
[105] R. Krishna, J.M. van Baten, Chem. Eng. J. 140 (2008) 614–620.
[106] E. Jolimaître, K. Ragil, M. Tayakout-Fayolle, C. Jallut, A.I.Ch.E.J. 48 (2002) 1927–1937.
[107] P.S. Bárcia, J.A.C. Silva, A.E. Rodrigues, Ind. Eng. Chem. Res. 45 (2006) 4316–4328.
[108] P.S. Bárcia, F. Zapata, J.A.C. Silva, A.E. Rodrigues, B. Chen, J. Phys. Chem. B 111 (2007) 6101–6103.
[109] Y. Ling, Z.X. Chen, F.P. Zhai, Y.M. Zhou, L.H. Weng, D.Y. Zhao, Chem. Commun. 47 (2011) 7197–7199.
[110] P.S. Bárcia, D. Guimarães, P.A.P. Mendes, J.A.C. Silva, V. Guillerm, H. Chevreau, C. Serre, A.E. Rodrigues, Microporous Mesoporous Mater. 139 (2011) 67–73.
[111] T. Maesen, T. Harris, Process for producing high RON gasoline using CFI zeolite, Chevron U.S.A. Inc, San Ramon, CA, US, US 70374222 B2, U.S., 2006.
[112] T. Maesen, T. Harris, Process for producing high RON gasoline using ATS zeolite, Chevron U.S.A. Inc, San Ramon, CA, US, US 7029572 B2, U.S., 2006.
[113] S.C. Xiang, Y. He, Z. Zhang, H. Wu, W. Zhou, R. Krishna, B. Chen, Nat. Commun. 3 (2012) 954. (http://dx.doi.org/doi:10.1038/ncomms1956).
[114] R. Krishna, J.M. van Baten, Sep. Purif. Technol. 87 (2012) 120–126.
[115] Y. Belmabkhout, G. Pirngruber, E. Jolimaitre, A. Methivier, Adsorption 13 (2007) 341–349.
[116] P. Nugent, Y. Belmabkhout, S.D. Burd, A.J. Cairns, R. Luebke, K. Forrest, T. Pham, S. Ma, B. Space, L. Wojtas, M. Eddaoudi, M.J. Zaworotko, Nature 495 (2013) 80–84.
[117] S. Vaesen, V. Guillerm, Q. Yang, A.D. Wiersum, B. Marszalek, B. Gil, A. Vimont, M. Daturi, T. Devic, P.L. Llewellyn, C. Serre, G. Maurin, G. De Weireld, Chem. Commun. 49 (2013) 10082–10084.
[118] R. Krishna, Microporous Mesoporous Mater. 156 (2012) 217–223.
[119] S. Couck, J.F.M. Denayer, G.V. Baron, T. Rémy, J. Gascon, F. Kapteijn, J. Am. Chem. Soc. 131 (2009) 6326–6327.
[120] S.M. Kuznicki, V.A. Bell, S. Nair, H.W. Hillhouse, R.M. Jacubinas, C.M. Braunbarth, B.H. Toby, M. Tsapatsis, Nature 412 (2001) 720–724.
[121] Z.R. Herm, J.A. Swisher, B. Smit, R. Krishna, J.R. Long, J. Am. Chem. Soc. 133 (2011) 5664–5667.
[122] J.A. Mason, K. Sumida, Z.R. Herm, R. Krishna, J.R. Long, Energy Environ. Sci. 4 (2011) 3030–3040.
[123] J. Duan, M. Higuchi, R. Krishna, T. Kiyonaga, Y. Tsutsumi, Y. Sato, Y. Kubota, M. Takata, S. Kitagawa, Chem. Sci. (2013) (http://dx.doi.org/10.1039/C3SC52177J)
[124] S. Yang, J. Sun, A.J. Ramirez-Cuesta, S.K. Callear, W.I.F. David, D.P. Anderson, R. Newby, A.J. Blake, J.E. Parker, C.C. Tang, M. Schröder, Nature Chemistry 4 (2012) 887–894.
[125] J.A. Delgado, M.A. Uguina, J.L. Sotelo, B. Ruíz, Sep. Purif. Technol. 49 (2006) 91–100.
[126] W. Lu, J.P. Sculley, D. Yuan, R. Krishna, H.C. Zhou, J. Phys. Chem. C 117 (2013) 4057–4061.
[127] T.M. McDonald, D.M. D'Alessandro, R. Krishna, J.R. Long, Chem. Sci. 2 (2011) 2022–2028.
[128] T.M. McDonald, W.R. Lee, J.A. Mason, B.M. Wiers, C.S. Hong, J.R. Long, J. Am. Chem. Soc. 134 (2012) 7056–7065.
[129] R. El Osta, A. Carlin-Sinclair, N. Guillou, R.I. Walton, F. Vermoortele, M. Maes, D. De Vos, F. Millange, Chem. Mater. 24 (2012) 2781–2791.
[130] M.A. Moreira, J.C. Santos, A.F.P. Ferreira, J. Loureiro, F. Ragon, P. Horcajada, K.E. Shim, Y.K. Hwang, U.H. Lee, J.S. Chang, C. Serre, A.E. Rodrigues, Langmuir 28 (2012) 5715–5723.
[131] M.A. Moreira, J.C. Santos, A.F.P. Ferreira, J. Loureiro, F. Ragon, P. Horcajada, P.G. Yot, C. Serre, A.E. Rodrigues, Langmuir 28 (2012) 3494–3502.
[132] M.A. Moreira, J.C. Santos, A.F.P. Ferreira, J. Loureiro, F. Ragon, P. Horcajada, P.G. Yot, C. Serre, A.E. Rodrigues, Microporous Mesoporous Mater. 158 (2012) 229–234.
[133] F. Vermoortele, M. Maes, P.Z. Moghadam, M.J. Lennox, F. Ragon, M. Boulhout, S. Biswas, K.G.M. Laurier, I. Beurroies, R. Denoyel, M. Roeffaers, N. Stock, T. Düren, C. Serre, D.E. De Vos, J. Am. Chem. Soc. 133 (2011) 18526–18529.
[134] M. Maes, F. Vermoortele, L. Alaerts, S. Couck, C.E.A. Kirschhock, J.F.M. Denayer, D.E. De Vos, J. Am. Chem. Soc. 132 (2010) 15277–15285.
[135] T. Remy, L. Ma, M. Maes, D.E. De Vos, G.V. Baron, J.F.M. Denayer, Ind. Eng. Chem. Res. 51 (2012) 14824–14833.
[136] A. Takahashi, R.T. Yang, A.I.Ch.E.J. 48 (2002) 1457–1468.
[137] H. Ren, T. Ben, E. Wang, X. Jing, M. Xue, B. Liu, Y. Cui, S. Qui, G. Zhu, Chem. Commun. 46 (2010) 291–293.
[138] S.J. Geier, J.A. Mason, E.D. Bloch, W.L. Queen, M.R. Hudson, C.M. Brown, J.R. Long, Chem. Sci. 4 (2013) 2054–2061.
[139] N. Lamia, M.A. Granato, P.S.A. Gomes, C.A. Grande, L. Wolff, P. Leflaive, D. Leinekugel-le-Cocq, A.E. Rodrigues, Sci. Technol. 44 (2009) 1485–1509.
[140] J. Van den Bergh, C. Gücüyener, E.A. Pidko, E.J.M. Hensen, J. Gascon, F. Kapteijn, Chem. Eur. J. 17 (2011) 8832–8840.
[141] M.C. Das, Q. Guo, Y. He, J. Kim, C.G. Zhao, K. Hong, S. Xiang, Z. Zhang, K.M. Thomas, R. Krishna, B. Chen, J. Am. Chem. Soc. 134 (2012) 8703–8710.
[142] Y. He, Z. Zhang, S. Xiang, F.R. Fronczek, R. Krishna, B. Chen, Chem. Commun. 48 (2012) 6493–6495.
[143] Y. He, S. Xiong, Z. Zhang, S. Xiong, F.R. Fronczek, R. Krishna, M. O'Keeffe, B. Chen, Chem. Commun. 48 (2012) 10856–10858.
[144] H. Xu, Y. He, Z. Zhang, S. Xiang, S. Xiong, J. Cai, Y. Cui, Y. Yang, G. Qian, B. Chen, J. Mater. Chem. A 1 (2013) 77–81.
[145] M. Fischer, F. Hoffmann, M. Fröba, ChemPhysChem 11 (2010) 2220–2229.
[146] R. Matsuda, R. Kitaura, S. Kitagawa, Y. Kubota, R.V. Belosludov, T.C. Kobayashi, H. Sakamoto, T. Chiba, M. Takata, Y. Kawazoe, Y. Mita, Nature 436 (2005) 238–241.
[147] A. Takahashi, R.T. Yang, C.L. Munson, D. Chinn, Ind. Eng. Chem. Res. 40 (2001) 3979–3988.
[148] T. Yamamoto, Y.H. Kim, B.C. Kim, A. Endo, N. Thongprachan, Chem. Eng. J. 181–182 (2012) 443–448.
[149] S. Sircar, A.L. Myers, Gas Separation by Zeolites, Chapter 22, S.M. Auerbach, K.A. Carrado and P.K. Dutta, Handbook of Zeolite Science and Technology, Marcel Dekker, New York, 2003.
[150] Y. Peng, Z. Zhang, X. Zheng, H. Wang, C. Xu, Q. Xiao, Y. Zhong, W. Zhu, Ind. Eng. Chem. Res. 49 (2010) 10009–10015.
[151] J. van den Bergh, W. Zhu, J. Gascon, J.A. Moulijn, F. Kapteijn, J. Membr. Sci. 316 (2008) 35–45.
[152] Y. Liu, G. Zeng, Y. Pan, Z. Lai, J. Membr. Sci. 379 (2011). 46-31.
[153] M.P. Bernal, J. Coronas, M. Menendez, J. Santamaria, A.I.Ch.E.J. 50 (2004) 127–135.
[154] Y. Hasegawa, T. Tanaka, K. Watanabe, B.H. Jeong, K. Kusakabe, S. Morooka, Korean J. Chem. Eng. 19 (2002) 309–313.
[155] J.C. White, P.K. Dutta, K. Shqau, H. Verweij, Langmuir 26 (2010) 10287–10293.
[156] H. Bux, C. Chmelik, J.M. Van Baten, R. Krishna, J. Caro, Adv. Mater. 22 (2010) 4741–4743.
[157] J. van den Bergh, W. Zhu, J.C. Groen, F. Kapteijn, J.A. Moulijn, K. Yajima, K. Nakayama, T. Tomita, S. Yoshida, Stud. Surf. Sci. Catal. 170 (2007) 1021–1027.
[158] T. Tomita, K. Nakayama, H. Sakai, Microporous Mesoporous Mater. 68 (2004) 71–75.
[159] S. Himeno, T. Tomita, K. Suzuki, K. Nakayama, S. Yoshida, Ind. Eng. Chem. Res. 46 (2007) 6989–6997.
[160] Y. Li, F. Liang, H. Bux, W. Yang, J. Caro, J. Membr. Sci. 354 (2010) 48–54.
[161] F. Zhang, X. Zou, X. Gao, S. Fan, F. Sun, H. Ren, G.S. Zhu, Adv. Funct. Mater. 22 (2012) 3583–3590.
[162] A. Huang, H. Bux, F. Steinbach, J. Caro, Angew. Chem., Int. Ed. 122 (2010) 5078–5081.
[163] H. Bux, A. Feldhoff, J. Cravillon, M. Wiebcke, Y.-S. Li, J. Caro, Chem. Mater. 23 (2011) 2262–2269.
[164] L. Diestel, X.L. Liu, Y.S. Li, W.S. Yang, J. Caro, Microporous Mesoporous Mater. (2013) (http://dx.doi.org/10.1016/j.micromeso.2013.09.012).
[165] I.G. Giannakopoulos, V. Nikolakis, Ind. Eng. Chem. Res. 44 (2005) 226–230.
[166] Y. Hasegawa, C. Abe, M. Nishioka, K. Sato, T. Nagase, T. Hanaoka, J. Membr. Sci. 364 (2010) 318–324.
[167] M. Pera-Titus, C. Fité, V. Sebastián, E. Lorente, J. Llorens, F. Cunill, Ind. Eng. Chem. Res. 47 (2008) 3213–3224.
[168] S. Khajavi, J.C. Jansen, F. Kapteijn, J. Membr. Sci. 326 (2009) 153–160.
[169] J. Kuhn, J.M. Castillo-Sanchez, J. Gascon, S. Calero, D. Dubbeldam, T.J.H. Vlugt, F. Kapteijn, J. Gross, J. Phys. Chem. C 113 (2009) 14290–14301.
[170] H. Voß, A. Diefenbacher, G. Schuch, H. Richter, I. Voigt, M. Noack, J. Caro, J. Membr. Sci. 329 (2009) 11–17.
[171] Z.A.E.P. Vroon, K. Keizer, M.J. Gilde, H. Verweij, A.J. Burggraaf, J. Membr. Sci. 113 (1996) 293–300.
[172] M. Arruebo, J.L. Falconer, R.D. Noble, J. Membr. Sci. 269 (2006) 171–176.

[173] C.J. Gump, R.D. Noble, J.L. Falconer, Ind. Eng. Chem. Res. 38 (1999) 2775–2781.
[174] K. Keizer, A.J. Burggraaf, Z.A.E.P. Vroon, H. Verweij, J. Membr. Sci. 147 (1998) 159–172.
[175] S. Sommer, T. Melin, J.F. Falconer, R.D. Noble, J. Membr. Sci. 224 (2003) 51–67.
[176] B.H. Jeong, Y. Hasegawa, K. Sotowa, K. Kusakabe, S. Morooka, J. Chem. Eng. Japan. 35 (2002) 167–172.